

Development of Deployable Arrays for Satellites through
Origami-Pattern Design, Modeling, and Optimization

Nathan M. Coleman

A thesis submitted to the faculty of
Brigham Young University
in partial fulfillment of the requirements for the degree of
Master of Science

Larry L. Howell, Chair
Spencer P. Magleby
Brian D. Jensen

Department of Mechanical Engineering
Brigham Young University

Copyright © 2024 Nathan M. Coleman

All Rights Reserved

*Development of Deployable
Arrays for Satellites through
Origami-Pattern Design,
Modeling, and Optimization*

Nathan M. Coleman
Department of Mechanical Engineering
Master of Science

BYU Engineering

Abstract

This research presents methods for modeling and optimizing an origami design using compliant mechanisms, improving origami design processes, modeling and analyzing rolling behavior of compliant designs, and an antenna design for SmallSats. A framework for the optimization of the origami Flasher pattern to mitigate issues with rigid-foldability is shown, and several optimization solutions are presented to overcome these issues. An alternative design method is presented which allows designers to more accurately predict the characteristics of a design in the deployed state, and configurations are shown for an example use case. A model for rolled gossamer structures is presented which predicts the relative slippage that adjacent panels will experience, and slippage trends are correlated with key pattern parameters. Finally, a SmallSat antenna design is presented, which stows compactly, incorporates a unique hinge design, utilizes magnets for stabilization in the deployed state, and self-deploys using compliant mechanisms.

Keywords: Deployable Arrays, Small Satellite Design, Origami, Compliant Mechanisms, Optimization

Acknowledgments

Thank you to my wife and best friend Brooklyn, for her constant support, patience, and laughter.

Thanks also to my advisor Dr. Larry Howell for his guidance, feedback, and counsel throughout my research, as well as my committee members Dr. Spencer Magleby and Dr. Brian Jensen for their support on this work.

This work has been funded by the Air Force Research Lab/U.S. Space Force, through award number FA9453-22-C-0013, and is also based on work supported by the Air Force Office of Scientific Research grant FA9550-19-1-0290 through Florida International University. This work has been supported by the Utah NASA Space Grant Consortium.

Additional thanks are given to Mitchel Skinner, Katie Varela, Jake Sutton, Ivy Running, Akash Biwas, Dr. Zhong You, Terri Bateman, Dr. Robert Lang, Dr. Denise Halverson, McKaelin Edralin, Dr. Collin Ynchausti, Hunter Pruett, Dr. Constantinos L. Zekios, Dr. Stavros V. Georgakopoulos, and Dr. John Salmon for their contributions to this work and as coauthors on associated publications.

Table of Contents

List of Figures	vii
List of Tables	xiii
Nomenclature	xiv
1 Introduction	1
2 A Framework for Origami-Flasher-Pattern Optimization	4
2.1 Introduction	4
2.2 Background	6
2.3 Methods	7
2.4 Results	14
2.5 Discussion	14
2.6 Conclusion	17
3 Designing Kirigami Patterns using the Hamiltonian Circuit Framework	18
3.1 Introduction	18
3.2 Background	19
3.3 Creating Folding Patterns	21
3.4 Additional Techniques	24
3.5 Applications in Patterns with Potential for Deployable Radio Frequency Arrays	26
3.6 Future Work	31
3.7 Conclusion	32
4 Modeling and Analysis of Slipping in Rolled Gossamer Arrays	33
4.1 Introduction	33
4.2 Background	33
4.3 Model	34
4.4 Simulation Results	40
4.5 Implementation	42
4.6 Conclusion	45
5 The KiHM-9: A Self-deploying PicoSat Antenna Design	46
5.1 Introduction	46

5.2	Design	47
5.3	Prototypes and Testing	52
5.4	Results	54
5.5	Conclusion	57
6	Conclusion	59
	References	61
	Appendices	66
A	Simplified Folding Model for Square-Based Patterns	67
B	KiHM-9 Manufacturing Details	69

List of Figures

- 2.1 Example Flasher configuration. (a) Stowed. (b) Partially deployed. (c) Deployed. 5
- 2.2 Example Cross-Frame Flasher configuration. Hinge locations are shown as red circles, and fall on the lines between original panel locations. (a) With Panels for reference. Note that the Cross-Frame intersects each frame edge line at its midpoint. (b) With no panels. 6
- 2.3 The Flasher configuration selected for the optimization with parameters $m = 4, r = 2, h = 2, dr = 0.2$. Note that mountain folds are shown as solid lines and valley folds are shown as dashed lines. Bisection lines are shown in light gray. 6
- 2.4 Illustration of initial Cross-Frame design. Note that frame structure is shown in green, panel outlines are shown in blue, and panel corners are shown in red. The dots around the edge indicate hinge placement. 8
- 2.5 Modified cross design, shown optimized to minimize total length of the beams. 8
- 2.6 Diamond frame design, shown optimized for stiffness. Bisection line is shown in dashed magenta. 9
- 2.7 Z-frame design, shown optimized for stiffness. Bisection line is shown in dashed magenta. 9
- 2.8 Cross design optimized to minimize total length of frame elements while varying locations of points along each panel edge and panel middle. 10
- 2.9 Diamond design optimized to minimize the ratio of stiffness across the bisection line to the stiffness across the non-bisection line, while varying locations of points along each panel edge. Note that this is done by minimizing the stiffness across the bisection line and maximizing the stiffness across the non-bisection line. 11
- 2.10 Z design optimized to minimize the ratio of stiffness across the bisection line to the stiffness across the non-bisection line, while varying locations of points along each panel edge. Note that this is done by minimizing the stiffness across the bisection line and maximizing the stiffness across the non-bisection line. 11

- 2.11 Model used for each of the beams within the optimized designs. 12
- 2.12 Full Flasher optimization shown overlaid with original pattern. 16
- 2.13 Prototype of the optimized diamond design. (a) Stowed. (b) Deployed. 16

- 3.1 Comparison between the final designs created using the bottom-up and top-down design methodologies. (a) Bottom-Up design methodology. (b) Top-Down design methodology. 19
- 3.2 Example of how a Hamiltonian circuit can be used to create a compactly stowing array which deploys out to a large area. (a) Circuit imposed on a square grid. (b) 3D printed prototype created from circuit, shown in deployed state. Note that the circle shown in the middle of the pattern is representative of the effective RF area of this pattern. Other patterns shown in later sections will also be shown with their effective RF areas for comparison. (c) 3D printed prototype created from circuit, shown in stowed state. 19
- 3.3 Example folding sequence for a kirigami pattern created using this methodology. 20
- 3.4 Example kirigami pattern selection using Hamiltonian circuits. Note that an unusual pattern was chosen to illustrate how a circuit may consist of an arbitrary group of grid cells. (a) Initial grid of hexagons. (b) Final deployed shape drawn onto grid. (c) Hamiltonian circuit drawn onto extracted shape. 21
- 3.5 Reflection sequence used to find valid fold groups. Fold group lines that do not cross the Hamiltonian circuit and will therefore not be used for folding are shown as dashed. 22
- 3.6 Fold groups created from unique pattern-circuit combination. All duplets of hexagons with identical colors are valid folding combinations with any other duplet of the same color. (a) Fold groups for selected kirigami pattern. Note that because the principal polygon was six sided, there are six unique fold groups. (b) All valid folding groups for selected kirigami pattern. 24
- 3.7 (a) Square-based pattern with 36-panels connected with a single closed loop. (b) Updated pattern after merging panels consisting of a closed loop and an open loop. 25

- 3.8 Explored patterns with example Hamiltonian circuits superimposed on top of each. Details of each pattern are given in Table 3.1. (a) 36-panel square pattern. (b) 32-panel square pattern. (c) Quasi-Octagon pattern. (d) 37-panel hexagonal pattern. (e) 19-panel hexagonal pattern. (f) Scale comparison of the circumscribed circle area of the each deployed pattern on the left, and a scale comparison of the stowed side and top area of each pattern on the right, with associated parameters. Dark blue corresponds with the 19-panel hexagonal pattern, light blue corresponds with the 37-panel hexagonal pattern, dark green corresponds with the Quasi-Octagon and 32-panel square patterns, and light green corresponds with the 36-panel square pattern. 27
- 3.9 Example implementation. (a) Valid Hamiltonian circuit for 32-panel square grid. (b) 3D printed prototype showing example of merged panels to reduce the overall degrees-of-freedom. (c) Valid Hamiltonian circuit for 19-panel hexagonal grid. Note that because the grid has an odd number of panels, one panel must be connected by a separate circuit on the back, shown in gray. (d) 3D printed prototype. 30
- 4.1 Example implementation of a gossamer pattern. (a) Deployed state, showing how a design may be visualized as a series of strips connected by hinges. In this example, there are 5 hinges connecting each set of adjacent panels. (b) Rolled state. This model is shown in the an additional possible rolled state in Fig.4.8. 34
- 4.2 Example figure of slipping that occurs during rolling. (a) Rolled book showing slipping between pages. The book shown (The Book of Mormon) has 531 pages. (b) Simulation model of book slippage. Model has 600 panels each with a thickness of 0.02 mm, a total length of 120 mm, and a minimum bend radius of 15 mm, as measured on the book. Because each membrane is so thin, it is difficult to distinguish layers in this example; however the model can be seen to align closely with the physical model, validating the rolling model used. (c) Simple example model to show individual panels. (d) Close-up showing slipping that occurs on the same point between panels in black. 35
- 4.3 Additional rolling models. (a) Exterior aligned, where the outer most edge of each sheet is kept aligned to its adjacent panel. (b) Centered, where the initial angle of each panel in the roll has been adjusted to balance the amount of slipping on each end of a panel, such that the slip on each end is kept equal. This reduces the maximum magnitude of the slippage on any panel. (c) Double roll, where each end is rolled towards the middle. 36

- 4.4 General array nomenclature. (a) Number of panels, length, and hinges definition figure. Hinges locations are shown as circles, indicating the point on each panel where slip is being measured. Note that the width of each panel does not affect the slipping between panels, as it is into the plane and does not affect the arc length being measured. (b) Thickness and minimum radius definition. 36
- 4.5 Interior aligned model with five hinges. (a) Model with given parameters, with hinge locations shown halfway through the slip measured for adjacent panels. (b) Plot of the magnitude of slip required at each hinge location. (c) Linear fit to the slippage plot. 39
- 4.6 Example heat maps showing how the maximum displacement changes for each combination of two parameters. For each combination, there are two parameters that change, and two parameters that are fixed. When fixed parameters are used in this example, there are thickness = 0.5, total length of each panel = 40, minimum bend radius = 1, and number of panels = 10. 42
- 4.7 Example heat maps showing how the slope of the linear fit changes for each combination of two parameters. For each combination, there are two parameters that change, and two parameters that are fixed. When fixed parameters are used in this example, there are thickness = 0.5, total length of each panel = 40, minimum bend radius = 1, and number of panels = 10. 43
- 4.8 Rolling model implementation with example hinges which can be used to accommodate slipping between panels. This model is shown in the open state in Fig. 4.1a. (a) Simulation model with the same parameters. Note that the red hinges in the model correspond to the white hinges in the prototype, the blue hinges in the model correspond to the gray hinges, and the green hinges in the model correspond to the black hinges in the prototype. Hinge colors were changed in the simulation to improve visibility. (b) Slip results for each hinge location in the simulation model. (c) Array in double rolled configuration. Note that the black hinges experience no slip, the gray hinges have some slip, and the white hinges on the outermost edges experience the most slip. (d) Simple hinge used to facilitate rotation and translational motion when stowed. 44
- 5.1 Initial deployed holographic metasurface antenna (HMA) concept design with 1U CubeSat structure. In the top left inset, the monopole that feeds the HMA is shown. In the bottom left inset, a $2mm$ sub-wavelength unit cell is shown consisting of a metallic square patch printed above a grounded substrate with a thickness of $1.57mm$. 47

- 5.2 (a) Analog flasher pattern with parameters $m=4$, $r=1$, $h=1$, and $dr=0$. Each repeating quadrant is referred to as a “gore”. (b) Associated kirigami flasher pattern. Mountain folds are shown with blue long dashed lines, valley folds are shown with red short dashed lines, and cut lines are shown with black solid lines. 48
- 5.3 Geometry of hinge structure from Ynchausti et al. Note that the thickness of the metasurface antenna panels is given by P , which is added to R_2 to give $R_{2, effective}$. 49
- 5.4 Close up of hinge design on final prototype. 51
- 5.5 (a) Lenticular fold which folds completely flat when stowed and provides an opening force. (b) Side view of the lenticular fold showing its deployed position and displacement relative to a stowed flat position. 53
- 5.6 (a) Panels used to tension and fatigue test the stainless steel mesh hinge. (b) Close-up photograph from a microscope used to inspect the mesh for material wear and deformation, 50 times zoom, after 100 open-close cycles. 54
- 5.7 The initial CubeSat prototype with deployable antenna structure, shown with one of its four gores attached. (a) Deployed structure with mock antenna panels attached. (b) Mock panels half-closed. The smaller magnets used for stabilization between panels are shown. (c) Mock panels stowed. The larger magnets used for stabilization between each gore to the CubeSat are shown. Note that all panels except for the central top panel are covered and protected during stowage. (d) Deployed structure with mock antenna panels removed to show screw attachment locations. Note the cutout in each of the 1a and 2a panels (defined in Appendix B, Fig. B.1) to reduce the weight of the overall structure as well as to tension the mesh during assembly. (e) Mock antenna panel with the same thickness as the proposed holographic metasurface antenna panels. (f) CubeSat attachment points on the top of the CubeSat. Threads are made with brass inserts in the 3D-printed CubeSat model. 55

- 5.8 The final CubeSat prototype with deployable mock antenna panels shown with all four gores attached. (a) The structure in the deployed configuration, shows a full pattern with 9 mock antenna panels. Note the high area-use efficiency. (b) The structure in deployed configuration, side view. Note that in micro-gravity the mock antenna structure achieves remarkable flatness using the magnets for stabilization and panel thickness as hard stops. (c) Stowed structure. A burn wire would be used to delay deployment until desired, and all panels besides the central panel are covered until deployed. (d) The final structure with mock antenna panels removed, showing the top geometry holding the mesh in place and the magnet placement on the center panel. (e) Final structure with mock antenna panels removed showing the geometry of each panel in the pattern. (f) Bottom view of the final antenna showing magnet placement underneath each panel, which is used to interlock and stabilize each gore. 56
- 5.9 (a) A holographic metasurface antenna without hinges; At the inset, the monopole that feeds the HMA is shown in a zoomed view. (b) Measurement setup, and (c) 2D normalized radiation pattern of the HMA prototype without hinges. (d) A fully deployed holographic metasurface antenna mounted on a CubeSat prototype. (e) Measurement setup, and (f) 2D normalized radiation pattern of the fully deployed HMA prototype mounted on a CubeSat prototype. 57
- A.1 (a) Reflection sequence used to find valid fold groups in square patterns. Fold group lines that do not cross the Hamiltonian circuit and will therefore not be used for folding are shown as dashed. (b) Simplified method shown in squares. 68
- B.1 Numbering nomenclature of the panels during manufacturing. Note that “a” refers the top half of the panel (associated with R_2 on panels 1 and 2) and “b” refers to the bottom half of the panel (associated with R_1 on panels 1 and 2). 69

List of Tables

- 2.1 Optimization Problem Formulation 13
- 3.1 Summary of Pattern Tradeoffs 31
- 3.2 Example weighted ranking method for determining preferred pattern 32
- 5.1 Fold pattern candidates based on patterns that can fold around 1U CubeSats. The red dashed lines are valley folds, the blue solid lines are mountain folds, and the interior black solid lines are cuts. The selected pattern is highlighted in blue. 47
- 5.2 Geometric variables of designed hinge. Items with an asterisk were given, and not determined through calculation. Note that f_1 is only necessary to facilitate manufacturing of the internal corner at the bottom R_1 . 51
- B.1 KiHM-9 Manufacturing Steps. 69
- B.2 KiHM-9 Bill of Materials. See Appendix I, Fig. B.1 for nomenclature on panel numbering. 70

Nomenclature

χ	Ratio of stiffnesses along bisection and non-bisection lines, respectively
\mathcal{L}	Total length of beam segments
τ	Minimum distance from a path end point to a panel vertex
θ	Angle between the beam element and the point moment vector [rad]
c	Associated with corner points for each panel
<i>Circuit</i>	A series of panels which are adjacent to each other, in which each panel is visited exactly once
<i>Duplet</i>	Two panels which are adjacent to a line of a folding set which intersects a given circuit
E	Modulus of elasticity [Pa]
e	Associated with edge points being optimized for each panel
G	Associated with opposite edge of a gore
I	Moment of inertia [kgm ²]
k	Rotational beam stiffness [Nm/rad]
L	Beam length [m]
$line_n$	Associated with edge lines for each panel
m	Associated with middle points being optimized for each panel
<i>Pair of Duplets</i>	Top and bottom duplets of a folded pattern which help define a circuit
q	Distance from edge of beam to point moment [m]

Introduction

The benefits of satellite technology are ubiquitous in the world today, enabling everyday needs such as communication, GPS, and weather forecasting. Satellites also have missions far from Earth, looking deep into the universe [1, 2], recording the makeup of distant celestial bodies [3, 4], and preparing mankind to visit new planets [5, 6]. The usage of space-based satellite systems has become increasingly common and the rate of new objects being launched into space has been increasing dramatically over the past few years [7, 8].

Satellites have a variety of onboard technology stemming from their specific mission requirements, such as solar arrays, LiDAR telescopes, and communication antennas. The performance of many types of mission-critical equipment is proportional to the amount of surface area that equipment has, such as the power generated by solar panels, the optical capability of telescope arrays, and signal transfer capability of RF antennas. It is therefore beneficial if these arrays can easily transform from a compact volume during launch into a large deployed area in space [9, 10]. Consequently, many spacecraft incorporate deployable arrays to maximize the area of these components in the limited volume available on launch, and an important focus of design has become increasing a spacecraft's ratio of deployed surface area to stowed volume to get the largest deployed array from the smallest launch payload. The design of mechanisms which can be deployed to a large surface from a small volume has been a goal of engineers for decades, and origami has proven to be a useful tool in achieving this goal [11, 12].

Principles of origami have been used to inspire deployable structures used in aerospace design, including a self-stiffening and retractable deployable space array [13], a foldable antenna [14–17], and a deployable Flasher-patterned solar array [18, 19]. This work addresses space-related applications of origami, but the principles here are not limited to those usages. Typically, deployable arrays are made out of interlinking panels that fold to a small volume before launch and can be deployed to a larger surface. This has led many to turn to the application of origami and kirigami (introducing cuts into an origami pattern) to aid in the folding of these arrays.

Another useful tool designers can use in conjunction with origami is compliance. Compliant mechanisms are mechanisms which derive some or all of their motion from the deflection of one or more members [20]. A

- [1] NASA, *James Webb Space Telescope*, 2024.
- [2] ESA, *Euclid*.
- [3] NASA, *Europa*, 2014.
- [4] ESA, *Cheops*.
- [5] NASA, *Mars Reconnaissance Orbiter*, 2024.
- [6] NASA, *Lunar Reconnaissance Orbiter*, 2024.
- [7] Outer Space Affairs, *Online Index of Objects Launched into Outer Space*, 2024.
- [8] Salas, *Number of satellites launched by year 2019, 2022*.
- [9] Rahmat-Samii *et al.*, "For Satellites, Think Small, Dream Big: A review of recent antenna developments for CubeSats." 2017.
- [10] Kaddour *et al.*, "A Foldable and Reconfigurable Monolithic Reflectarray for Space Applications," 2020.
- [11] Filipov *et al.*, "Origami tubes assembled into stiff, yet reconfigurable structures and metamaterials," 2015.
- [12] Kuribayashi *et al.*, "Self-deployable origami stent grafts as a biomedical application of Ni-rich TiNi shape memory alloy foil," 2006.
- [13] Pehrson *et al.*, *Self-deployable, self-stiffening, and retractable origami-based arrays for spacecraft*, 2020.
- [14] Liu *et al.*, "A design of an origami reconfigurable QHA with a foldable reflector [antenna applications corner]," 2017.
- [15] Kaddour *et al.*, "A reconfigurable origami reflectarray," 2020.
- [16] Russo *et al.*, "A Capacity Reconfigurable Multimode Origami MIMO Antenna," 2019.
- [17] Lee *et al.*, "Frequency-reconfigurable antenna inspired by origami flasher," 2019.
- [18] Zirbel *et al.*, "Accommodating thickness in origami-based deployable arrays," 2013.
- [19] Guang *et al.*, "An approach to designing deployable mechanisms based on rigid modified origami flashers," 2018.
- [20] Howell, *Compliant mechanisms*, 2001.

simpler way of saying this is compliant mechanisms are designed to flex and bend, whereas traditional mechanisms would be rigid. Compliant mechanisms are particularly ideal candidates for space-based designs as they have the following benefits:

1. Precise motion from a lack of backlash, less wear, and no friction in the mechanism
2. Predictable performance over a long period of time
3. Reduced part count reduces the complexity of designs and mass of mechanisms launched into space
4. Reduced price due to fewer parts required and reduced assembly

The origami Flasher pattern is a promising design for use in deployable space-based systems for its circular nature and fixed central polygon, which lend themselves to uses with reflectarray communication systems and grounding to satellites. One complication with the Flasher pattern is its inability to rigidly fold. Chapter 2 demonstrates a framework for the optimization of the origami Flasher pattern to mitigate these rigid-foldability issues. This work was published in the 47th Mechanisms and Robotics Conference (MR) at the International Design Engineering Technical Conferences and Computers and Information in Engineering Conference (IDETC-CIE) [21].

When creating a deployable design using origami, it is common to begin with a zero-thickness pattern, to which a thickness accommodation technique [22] is then applied to allow for the thickness of the panels in the design, as described by Bolanos et al. [23] An interesting characteristic of design using origami patterns is that the same origami pattern can result in many different final designs and shapes, dependent on the thickness accommodation technique chosen. This can make determining the final configuration of these designs at the beginning of the design process more challenging. This approach is referred to as a bottom-up method, and results in various mechanical systems, with varying shapes, degrees of stowed volume efficiency, and deployed area efficiency. Chapter 3 builds on an approach (referred to as a top-down design method) using Hamiltonian circuit framework, which allows a designer to choose a final deployed shape and aspect ratio, and then determine a corresponding kirigami pattern. This work is in review for publication in the 2024 International Conference on Reconfigurable Mechanisms and Robots (ReMAR) [24].

Gossamer structures are structures made from thin membranes, and address the tradeoff between increased surface area and smaller stowed volumes by creating arrays which are typically lightweight and have a low stiffness. Gossamer structures have been used by space agencies as far back as the 1950s [25], and their development continues to generate research and applications, including inflatable, ribbed, tensioned, parabolic, wrinkled, reflectors, sails, solar arrays, and

[21] Coleman *et al.*, *A Framework for Origami Flasher Pattern Optimization to Mitigate Rigid-Foldability Issues*, 2023.

[22] Lang *et al.*, "A review of thickness-accommodation techniques in origami-inspired engineering," 2018.

[23] Bolanos *et al.*, *A Preliminary Approach to Select an Origami Source Pattern for Deployable Space Arrays*, 2022.

[24] Coleman *et al.*, *A Methodology for Designing and Improving Novel Kirigami Patterns using the Hamiltonian Circuit Framework (In-Review)*, 2024.

[25] Jenkins, *Gossamer spacecraft: membrane and inflatable structures technology for space applications*, 2001.

[26] Chandra *et al.*, "A review on developments of deployable membrane-based reflector antennas," 2021.

[27] Arya *et al.*, "Ultralight structures for space solar power satellites," 2016.

[28] Fang *et al.*, "Development of a 7-meter inflatable reflectarray antenna," 2004.

[29] Seefeldt *et al.*, "Gossamer-1: Mission concept and technology for a controlled deployment of gossamer spacecraft," 2017.

[30] Ruggiero *et al.*, "Gossamer spacecraft: recent trends in design, analysis, experimentation, and control," 2006.

[31] Furuya *et al.*, "Manufacturing and Folding of Solar Sail 'IKAROS'," 2011.

optical gossamer structures [26–31]. Chapter 4 demonstrates a model for the inter-panel slipping that occurs when rolling gossamer structures, and analyzes the tradeoffs between the primary design parameters. This work is in review for publication in the 48th Mechanisms and Robotics Conference (MR) at the International Design Engineering Technical Conferences and Computers and Information in Engineering Conference (IDETC-CIE) [32].

One factor that has contributed to the increase in satellite launches each year is that technology has allowed satellites to become increasingly lighter and, therefore, less expensive to launch. An example of how satellites have become lighter is the advent of the CubeSat, which first launched in 2003 and has since become a standard platform for simple space missions [33–35].

Chapter 5 addresses the popularity of smallsats by creating and demonstrating a holographic metasurface antenna (HMA) design for smallsats that stows compactly, incorporates a unique surrogate hinge design, magnetic stabilization design, and deployment method. This work was presented and published with the American Institute of Aeronautics and Astronautics (AIAA) SciTech 2024 Forum session on Small Satellite Deployable Structures [36].

This research presents methods for modeling and optimizing an origami design using compliant mechanisms, improving origami design processes, modeling and analyzing rolling behavior of compliant designs, and an antenna design for SmallSats.

[32] Coleman *et al.*, *Modeling and Analysis of Inter-Panel Slipping for the Design of Rolled Gossamer Arrays (In-Review)*, 2024.

[33] Toorian *et al.*, "The CubeSat Approach to Space Access," 2008.

[34] Lokman *et al.*, "A review of antennas for picosatellite applications," 2017.

[35] Liu *et al.*, "Review of large spacecraft deployable membrane antenna structures," 2017.

[36] Coleman *et al.*, *The KIHM-9: A Self-Deploying Picosat Holographic Metasurface Antenna (HMA) Design*.

A Framework for Origami-Flasher-Pattern Optimization

Origami is increasingly popular in engineering for its ability to deploy to a large area from a compact volume. In addition to its circular nature and fixed central polygon, the origami Flasher pattern has several advantages that make it a desirable candidate for many deployable systems, including space applications such as LiDAR telescopes, solar arrays, or reflectarray antennas. Some complications with the Flasher pattern that limit its application are panel interference due to multiple high degree vertices and its inability to rigidly fold. This work builds on the Cross-Frame design by Varela et al., which was implemented as a thickness accommodation technique, as well as a solution for the interference issues. Modifications of the Cross-Frame design for the Flasher origami pattern are presented, which address interference and the rigid-foldability issues within the Flasher pattern. Three frame designs, the modified cross, the diamond, and the Z design, are presented and trade-offs for each design regarding stiffness, either localized or generalized, are explored. Methods for optimizing each frame design to accommodate for rigid-foldability are introduced and algorithms and constraints for this topological optimization are discussed. Results of optimizations for stiffness and length are shown, and further modifications for future research are discussed. This chapter is based on work published with Katie Varela, Mitchel Skinner, Larry L. Howell, and Spencer P. Magleby in the 47th Mechanisms and Robotics Conference (MR) at the International Design Engineering Technical Conferences and Computers and Information in Engineering Conference (IDETC-CIE) [21].

2.1 Introduction

Folded mechanical systems based on origami patterns have the ability to change their shape during their folding or unfolding process. This ability has often been used to compactly stow large arrays [11], though origami-based designs have recently been used for many additional engineering applications [12, 20]. Principles of origami have been used to inspire deployable structures used in aerospace design, including a self-stiffening and retractable deployable space array [13], a foldable antenna [14–17], and a deployable Flasher-patterned solar array [18, 19]. This work will address space-related applications of origami, but the

[21] Coleman et al., *A Framework for Origami Flasher Pattern Optimization to Mitigate Rigid-Foldability Issues*, 2023.

[11] Filipov et al., "Origami tubes assembled into stiff, yet reconfigurable structures and metamaterials," 2015.

[12] Kuribayashi et al., "Self-deployable origami stent grafts as a biomedical application of Ni-rich TiNi shape memory alloy foil," 2006.

[20] Howell, *Compliant mechanisms*, 2001.

[13] Pehrson et al., *Self-deployable, self-stiffening, and retractable origami-based arrays for spacecraft*, 2020.

[14] Liu et al., "A design of an origami reconfigurable QHA with a foldable reflector [antenna applications corner]," 2017.

[15] Kaddour et al., "A reconfigurable origami reflectarray," 2020.

[16] Russo et al., "A Capacity Reconfigurable Multimode Origami MIMO Antenna," 2019.

[17] Lee et al., "Frequency-reconfigurable antenna inspired by origami flasher," 2019.

[18] Zirbel et al., "Accommodating thickness in origami-based deployable arrays," 2013.

[19] Guang et al., "An approach to designing deployable mechanisms based on rigid modified origami flashers," 2018.

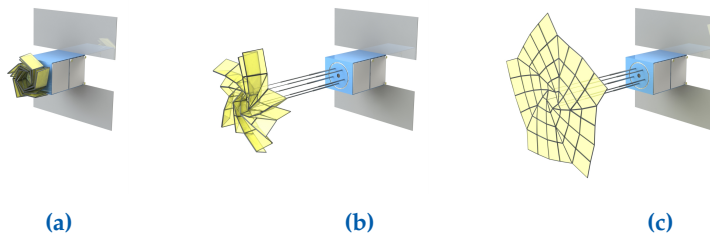


Figure 2.1: Example Flasher configuration. (a) Stowed. (b) Partially deployed. (c) Deployed.

principles here are not limited to those usages.

Many space applications, such as solar arrays, reflectarray antennas, and LiDAR telescopes, require large, flat surface areas. Therefore, these arrays need to be able to easily transform from a compact volume into a relatively large deployed area. Because origami patterns tend to be compact when stowed, they can be well suited for space applications.

An origami pattern that has been of interest for space and other applications is called the Flasher [19, 37–39]. An example of Flasher deployment is shown in Fig. 2.1. This pattern’s key benefit is its ability to be compact when stowed, then open to have an array with a large area-to-volume ratio. Other benefits of the Flasher include that it is generally circular in nature, extensible by adding more rings, and has a central panel that can be used for anchoring. The Flasher is not a flat-folding pattern, but instead wraps around itself as it is stowed, achieving a flat state only when fully deployed. The Flasher is also not rigid-foldable.

Tachi describes rigid-foldable origami (or rigid origami) as “piecewise linear origami that is continuously transformable without the deformation of each facet” [40]. In other words, if a panel is not rigid-foldable, the panel itself must deform or bend during the transition between stowed and deployed, instead of having all of the motion in the folds [40–42].

The Flasher pattern was adapted to create a solar array, using a membrane hinge approach that reduced the rigid-foldability complications [18, 39]. Additional work has been done to accommodate thickness in the Flasher for other space-related applications [43, 44], because using materials with any finite thickness affects the pattern’s ability to fold [22].

This work modifies structural topology of Flasher panels to help address the complications due to rigid-foldability. The model was proposed by Varela et al. [44], called the Cross-Frame, and is used for both thickness accommodation and structural support for the Flasher array. That initial work puts the frames through the center of the panels, preventing interference issues by keeping material away from the vertices, as shown in Fig. 2.2. This paper considers topological features to reduce issues with rigid-foldability by modifying the geometry (similarly implementing the principle that link shape does not matter for kinematic motion), but does not address thickness accommodation directly.

The objective of this work was to create a framework to optimize

[19] Guang *et al.*, “An approach to designing deployable mechanisms based on rigid modified origami flashers,” 2018.

[37] Srinivas *et al.*, “Directing acoustic energy by flasher-based origami inspired arrays,” 2020.

[38] Lang *et al.*, “Single degree-of-freedom rigidly foldable cut origami flashers,” 2016.

[39] Zirbel, “Compliant Mechanisms for Deployable Space Systems,” 2014.

[40] Tachi *et al.*, “Rigid-foldable thick origami,” 2011.

[40] Tachi *et al.*, “Rigid-foldable thick origami,” 2011.

[41] Watanabe *et al.*, “The method for judging rigid foldability,” 2009.

[42] Akitaya *et al.*, “Rigid foldability is NP-hard,” 2018.

[18] Zirbel *et al.*, “Accommodating thickness in origami-based deployable arrays,” 2013.

[39] Zirbel, “Compliant Mechanisms for Deployable Space Systems,” 2014.

[43] Bolanos *et al.*, “Selecting and Optimizing Origami Flasher Pattern Configurations for Finite-Thickness Deployable Space Arrays,” 2022.

[44] Varela *et al.*, “Thickness Accommodation for the Flasher Origami Deployable Array,” 2023.

[22] Lang *et al.*, “A review of thickness-accommodation techniques in origami-inspired engineering,” 2018.

[44] Varela *et al.*, “Thickness Accommodation for the Flasher Origami Deployable Array,” 2023.

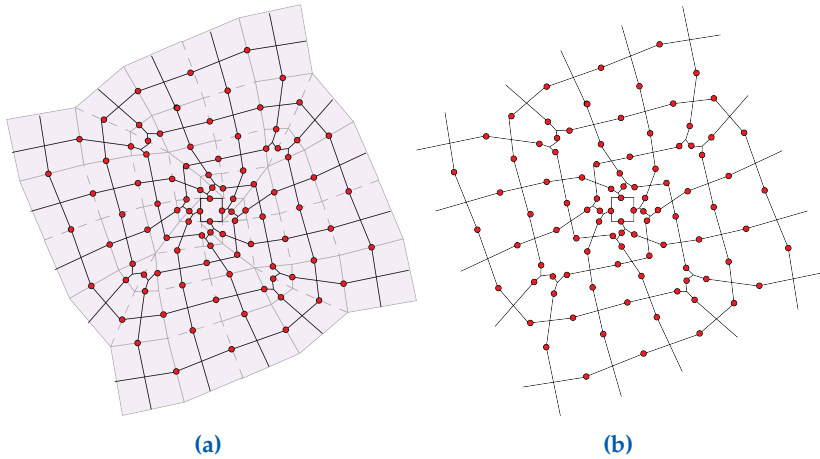


Figure 2.2: Example Cross-Frame Flasher configuration. Hinge locations are shown as red circles, and fall on the lines between original panel locations. (a) With Panels for reference. Note that the Cross-Frame intersects each frame edge line at its midpoint. (b) With no panels.

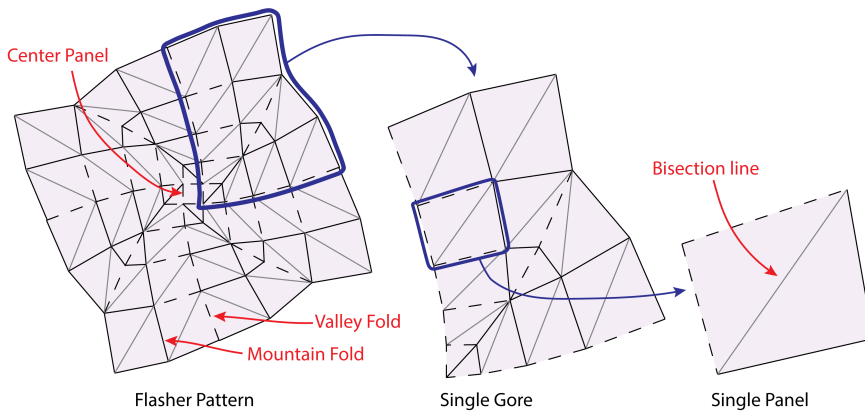


Figure 2.3: The Flasher configuration selected for the optimization with parameters $m = 4$, $r = 2$, $h = 2$, $dr = 0.2$. Note that mountain folds are shown as solid lines and valley folds are shown as dashed lines. Bisection lines are shown in light gray.

the structural support for the Flasher panels so that they can deflect as needed, while maintaining the stiffness of the array in the deployed state. In other words, to create a localized region of stiffness in the panel, so the panel can be flexible in one direction, but stiff overall. In this work, the compliance of the panel geometry achieves a slight deflection along the bisection line (shown in Fig. 2.3), which allows the pattern to fold with semi-rigidity, while maintaining the original number of panels, fold lines, and degrees of freedom as the origami pattern.

2.2 Background

The Flasher has four parameters that describe its configuration: m , r , h , and dr , which are described in detail by Zirbel et al. [18] For this optimization, the Flasher selected has parameter values of $m = 4$, $r = 2$, $h = 2$, and $dr = 0.2$, as shown in Fig. 2.3. These parameters were chosen

[18] Zirbel et al., "Accommodating thickness in origami-based deployable arrays," 2013.

because they represent a Flasher with a typical deployed area to stowed volume ratio. Because $m = 4$, the Flasher has four repeating sections, called gores, that have rotational symmetry.

2.2.1 Rigid-Foldability

Previous work done to accommodate for rigid-foldability issues when folding added a bisection line along each quadrilateral panel, making the pattern rigid-foldable [45], but increasing the total number of panels and complexity of the pattern. Another method to address this involves kirigami, or origami with cuts, which adds additional degrees of freedom into the system, negating one of the major benefits of using origami to begin with [17]. To maintain the simplicity of the original pattern, this work has developed an optimization framework which reduces the bending stiffness of each panel along the bisection line given by Lang [45] and maximizes the stiffness in the pattern in the other direction, referred to as the non-bisection direction.

[45] Lang, *Tessellatica*, 2021.

[17] Lee *et al.*, "Frequency-reconfigurable antenna inspired by origami flasher," 2019.

[45] Lang, *Tessellatica*, 2021.

2.2.2 Compliant Mechanisms

Compliant mechanisms are mechanisms which derive some or all of their motion through the deflection of their members [20]. These mechanisms can be modelled using the pseudo-rigid body model, which allow them to be analyzed as rigid bars and torsional springs with stiffness k , which depend on their material, geometry, and end conditions. The stiffness of these members is inversely proportional to their length, as shown in the Equations 2.1 and 2.2. By modeling the frame elements of the modified Cross-Frame Flasher as simply supported beams, the frame elements of each panel may be treated as springs in parallel, and the stiffness of the panel can be found by adding up the stiffnesses of each frame element of that panel. According to this assumption, the stiffness along the bisection line may be minimized by minimizing the number of beams in that direction and increasing their length, and the stiffness along the non-bisection line may be maximized by increasing the number of beams in that direction and minimizing their length, among other parameters.

[20] Howell, *Compliant mechanisms*, 2001.

2.3 Methods

2.3.1 Overview

The design approach behind the Cross-Frame Flasher seeks to take a panel made up of a regular polygon with three or four sides and shift the structure away from the vertices to avoid complications during thickness accommodation and folding. Fig. 2.2 shows this approach applied to a full Flasher pattern and Fig. 2.4 shows a single panel from that Flasher pattern.

Because these panels need to be able to connect to each other, it is necessary to have at least one hinge along each panel edge. The work done by Varela *et al.* [44] applied this methodology to an entire Flasher by placing the Cross-Frame at the center of each panel polygon, or in

[44] Varela *et al.*, "Thickness Accommodation for the Flasher Origami Deployable Array," 2023.

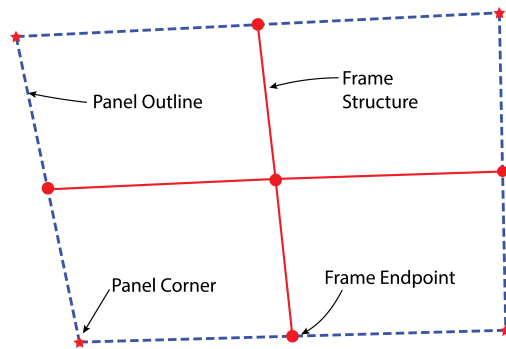


Figure 2.4: Illustration of initial Cross-Frame design. Note that frame structure is shown in green, panel outlines are shown in blue, and panel corners are shown in red. The dots around the edge indicate hinge placement.

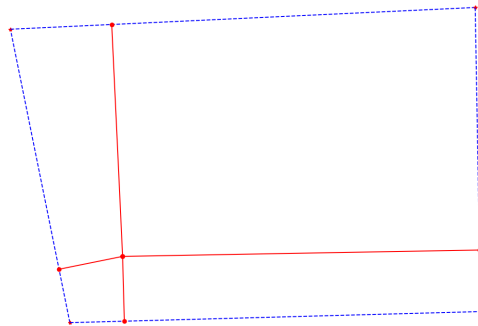


Figure 2.5: Modified cross design, shown optimized to minimize total length of the beams.

other words, having the hinge locations at the midpoints of each edge, shown in Fig. 2.4.

This work sought to build on the original Cross-Frame by optimizing the placement of the elements within each panel using three different methods, called “the optimized cross”, “the diamond”, and “the Z frame”, shown in Figs. 2.5, 2.6, and 2.7, respectively. These three designs were derived from the condition that each panel must connect to each adjacent panel by at least one point, and as such all contain one point along each panel edge, although they differ in how they connect the edge points.

The model used here initially sought to minimize the total length of the frame, which was used as a surrogate for maximizing the overall stiffness due to the inverse relationship between length and stiffness. From this criterion, the optimized cross design was created by selecting points for the hinge locations and the middle point that would minimize each beam’s length. Because of this modification, a major difference between this design and the original Cross-Frame design is that cross elements are not constrained to be at the midpoint of the panel edges. An example of the modified cross design is shown in Fig. 2.5.

However, because the Flasher design requires bisections on quadrilat-

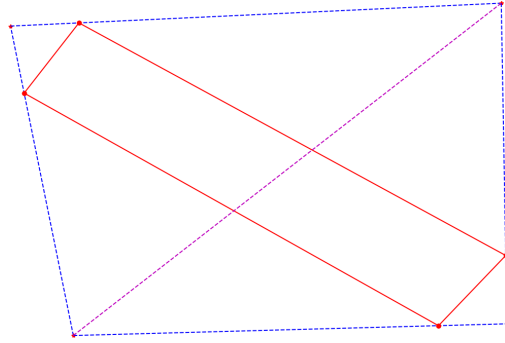


Figure 2.6: Diamond frame design, shown optimized for stiffness. Bisection line is shown in dashed magenta.

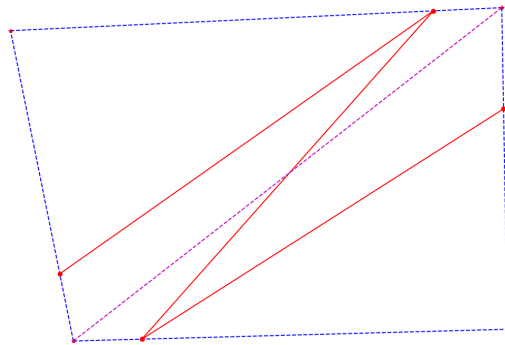


Figure 2.7: Z-frame design, shown optimized for stiffness. Bisection line is shown in dashed magenta.

eral panels in order to be rigid-foldable, the objective was not to maximize the stiffness of every panel, but rather to minimize the stiffness of the frame along the bisection axis and stiffen it in the axis opposite to the bisection. These diagonals are predefined by the pattern, or the panel boundaries themselves, and do not change with the shape of the support structure. This constraint led to the development of two different designs which include no middle point and connect the edge points directly to each other.

The first is referred to as the “diamond frame” design, in which the frame makes a diamond shape in connecting to all edge points, shown in Fig. 2.6. This design was derived from basic compliant mechanism principles - long members flex more than short members (with the same material, cross-section, applied force/moment, etc.) [20], and therefore, it uses short beams in the directions that require stiffness and longer beams in the directions that require flexibility. The diamond design has an analytical advantage of maintaining an overall stiffness for each panel while allowing for reduced stiffness along one axis.

The second design without a central connection point is referred to as the “Z frame” design (see Fig. 2.7), which functions according to the same principle as the diamond, but uses only three members to connect all four sides. The theory behind this design is that it minimizes the frame structure required to connect each panel, though this could make it less

[20] Howell, *Compliant mechanisms*, 2001.

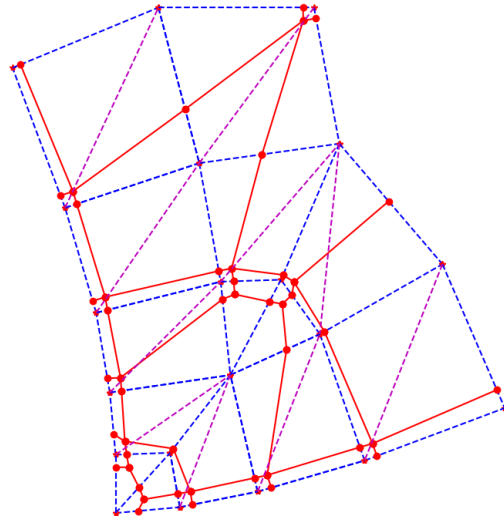


Figure 2.8: Cross design optimized to minimize total length of frame elements while varying locations of points along each panel edge and panel middle.

stiff overall. It can be noted that there are four possible Z orientations to connect the edge points of each panel, and the orientation chosen reflects the minimization of stiffness in the desired direction to aid in folding.

Each of these three panel frame designs were used and compared in the optimization of the full Flasher to compare the advantages and disadvantages of each. Once the optimization of each panel was set up, adjacent panels could be optimized together by having the panels share common edge points. This approach was used to optimize an entire gore of the Flasher for each frame design described, as shown in Figs. 2.8, 2.9, and 2.10. The optimization of a single gore of the Flasher was able to be used as a surrogate for the entire Flasher by adding an additional constraint to keep points on the edge of the gore aligned with their corresponding points on the opposite edge.

Once the optimization was found to be working correctly for each method with a full Flasher, various stiffness models were analyzed for their potential implementation, and a relative stiffness model was chosen. To accomplish the goal of achieving stiffness in all directions except along the bisection line, the optimization was able to vary the x and y positions of all points along the sides of each panel, subject to the polygon boundaries, the panel edge lines, minimum distance constraints between points, and symmetry between gore edges.

2.3.2 Analytical Stiffness Model

Calculating the stiffness of these structures is complicated by the variety of configurations that can be utilized, and the boundary conditions depend somewhat on the selected configuration. For this work, a simply supported beam with a point moment on the beam span was selected as the basic model, as shown in Fig. 2.11.

It was assumed that the magnitude of the moment caused by the panel bending would be equivalent on each beam, and that the vector

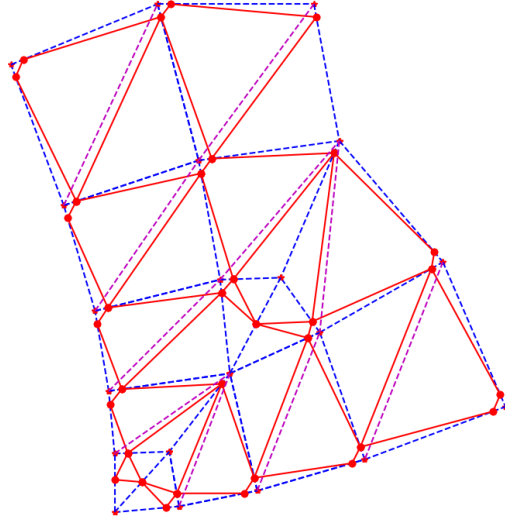


Figure 2.9: Diamond design optimized to minimize the ratio of stiffness across the bisection line to the stiffness across the non-bisection line, while varying locations of points along each panel edge. Note that this is done by minimizing the stiffness across the bisection line and maximizing the stiffness across the non-bisection line.

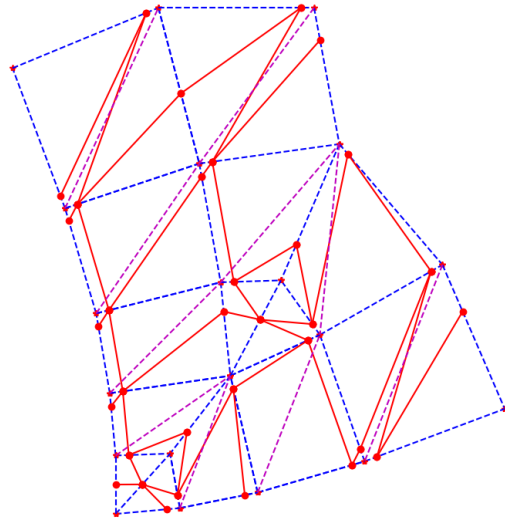


Figure 2.10: Z design optimized to minimize the ratio of stiffness across the bisection line to the stiffness across the non-bisection line, while varying locations of points along each panel edge. Note that this is done by minimizing the stiffness across the bisection line and maximizing the stiffness across the non-bisection line.

component that is parallel to the beam (causing torsion) is negligible compared to the bending component. With these assumptions and a fixed cross-section and material, the stiffness equation $k = M/\theta$ is the general form for stiffness with bending moments, so the equations for M and θ associated with a simply supported beam with a point moment at an arbitrary distance were substituted in, which simplifies to

$$k_q = \frac{3EIL \sin \theta}{L^2 - 3Lq + 3q^2} \quad (2.1)$$

where the bending moment component, $\sin \theta$, is determined by the angle

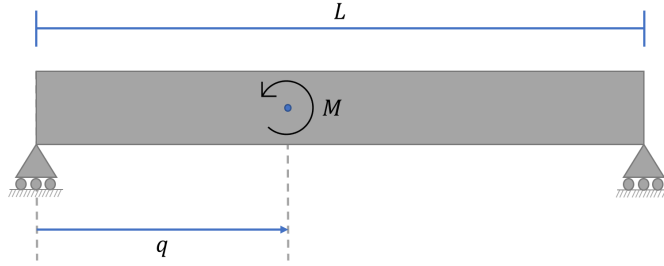


Figure 2.11: Model used for each of the beams within the optimized designs.

that is made between the beam element and the moment vector. The variable q is defined as

$$q = RL \quad (2.2)$$

where R is a fraction that describes how far along the beam the moment is acting, and $R \in [0, 1]$. Because of the symmetry, it does not matter whether q is measured from the “left” or the “right” end of the beam, so RL can be substituted for q , allowing the Equation 2.1 to simplify further, canceling out the L in the numerator by factoring an L from each term in the denominator. This factor also weights the equations to get a maximum stiffness by applying the moment at the center of the beam, and a minimum by applying the moment at the edges.

A ratio of the stiffnesses was calculated along the bisection line versus along the “non-bisection” line, as shown in Equation 2.3 below. By using a ratio of stiffness, the assumptions of the beam end conditions, as well as values for modulus of elasticity and moment of inertia of the beam, will be present in both the numerator and the denominator and therefore cancel out and not affect the calculated result. The resulting stiffness ratio, χ , is

$$\chi = \frac{k_{Bisection}}{k_{Non-Bisection}} = \frac{L_{NB}(1 + 3R_{NB} + 3R_{NB}^2) \sin \theta_B}{L_B(1 + 3R_B + 3R_B^2) \sin \theta_{NB}} \quad (2.3)$$

Equation 2.3 will be used as the objective function, which will minimize the stiffness along the bisection line and maximize the stiffness along the other diagonal by varying L , R , and θ for both diagonals.

Because the modified cross method yielded segments that do not intersect with either the bisection or non-bisection lines, the stiffness calculation ratio described above is not effective. Therefore, the cross structure shown in Fig. 2.8 only minimizes length, and does not have stiffness ratios associated with it. Additionally, for all three designs, the triangular panels in each gore do not have bisection lines, so they also were calculated to minimize length, since they do not need to flex during deployment, and therefore can have maximum stiffness.

2.3.3 Optimization Details

The problem formulation used to optimize the frame of a single panel and a full Flasher gore is given in Table 2.1, which minimizes the objective

function given in Equation 2.3, subject to constraints 1-6. This same method was used for optimizing the entire Flasher, with the addition of constraint 7, which keeps adjacent Flasher gores aligned. Note that constraints 1 and 7 are equality constraints, while constraints 2 through 6 are inequality constraints.

To optimize the pattern, initial guesses were selected for each point using the midpoint of the corresponding panel edge. Additionally, for the optimized cross, the initial guess for the center point was determined from the middle of the panel. It should be noted that single-panel optimizations using the listed constraints presented several equivalent local minima when optimizing for length, and as such, it should be acknowledged that the optimization of full Flasher gore represents one of several potential configurations. To account for this, additional constraints should be added for thickness accommodation, manufacturing, and general feasibility as needed. Because each gore is identical, the optimization is determined for panels on one gore, with considerations (via constraints) of how each gore would connect to the next. Note that the gores are staggered as they wrap around the central polygon, which the optimization also takes into account.

Constraint 1 is used to keep each optimal edge point on its associated panel edge line. Constraint 2 is used to keep each optimal middle point (when using the modified cross pattern) within the bounds of its associated panel.

Constraints 3 through 6 use Euclidean distance to avoid trivial solutions where multiple points are at the same location or points are at panel vertices. These are necessary to maintain the benefit of the Cross-Frame design by creating space between the frame and the panel vertices to avoid interference issues at each vertex. The parameter “ τ ” is used to define the minimum allowable distance between points. Constraint 3 compares each hinge location to every other hinge location, to make sure they do not find the same optimal position. Although this constraint recommends that every hinge point be checked for the minimum distance, the speed of the optimization can be significantly improved by checking only the “nearest neighbors” or adjacent points. Note that

Table 2.1: Optimization Problem Formulation

minimize	χ	
by varying	$(x, y)_e$	
subject to	$(x, y)_e \in line_n$	(1)
	$(x, y)_m \in (x, y)_c$	(2)
	$\ (x, y)_{e_i} - (x, y)_{e_j}\ _2 \geq \tau, \text{ for } i \neq j$	(3)
	$\ (x, y)_e - (x, y)_m\ _2 \geq \tau$	(4)
	$\ (x, y)_e - (x, y)_c\ _2 \geq \tau$	(5)
	$\ (x, y)_m - (x, y)_c\ _2 \geq \tau$	(6)
	$\ (x, y)_e - (x, y)_c\ _2 = \ (x, y)_e^G - (x, y)_c^G\ _2$	(7)

constraint 3 does not check each edge point against itself. Constraint 4 is applicable only for the modified cross design, and determines if the distance between the middle point and the edge points is smaller than τ . Constraints 5 and 6 check if the edge points and middle points (again, only for the modified cross approach) are far enough away from the corners of their panel, respectively.

Constraint 7 also uses Euclidean distance (or 2-norm) to extrapolate the optimization of a single gore out to the entire Flasher by constraining the optimal points on the edges of the each gore to be at equal distances from their associated corners; in other words, this algorithm ensures that the connection points from gore to gore will align with each other in order to create a continuous frame.

The optimization algorithm used in this work was the python SciPy “minimize” package, and the supplementary algorithms that were created for the constraints are not included in this work for conciseness.

2.4 Results

For the diamond and the Z methods, the optimizer was effectively able to vary L , R , and θ for each of the diagonals, maximizing L_B , R_B , and $\sin \theta_{NB}$ and minimizing L_{NB} , R_{NB} , and $\sin \theta_B$, as shown in Equation 2.3. Observations of the resulting optimizations demonstrated that the R values and the $\sin \theta$ values were driving factors, particularly in the diamond method (see Fig. 2.9).

The resulting optimized gores for each frame design can be seen in Figs. 2.8- 2.10. Note that the bisection lines are shown in red for Figs. 2.9 and 2.10, but not for Fig. 2.8, because the modified cross design was not optimized around stiffness. These results from the single panel optimizations suggest that this framework is a valid method for implementing compliance into rigid-foldable origami patterns.

2.5 Discussion

2.5.1 Modified Cross Design

Length minimization was used for the modified cross design. The results in Fig. 2.8 brought the cross intersection point as close to a vertex as possible (considering the constraints), and often had most of the hinge points surrounding a vertex. For this design, the results were mostly intuitive, though because all the panels needed to connect with each other, there are some angles that were less obvious. Still, this optimization was able to maintain the space around the vertices, especially around the degree-six vertex that has the most interference. This method was not modified for bisection line flexibility, so no conclusions will be drawn regarding that objective.

The modified cross design, because it does not have an accurate stiffness ratio, is not recommended for addressing the issue with rigid-foldability. However, a different stiffness calculation method could be utilized to achieve this objective.

2.5.2 Diamond Design

The results of the single gore optimization with the diamond design are shown in Fig. 2.9. Comparing these results to the single panel optimization shown in Fig. 2.6, the frame of each panel in the full gore are noticeably more trapezoidal. This was not an anticipated result, but can be verified through Equation 2.3, as the optimizer determined that the R and $\sin \theta$ terms contributed more than the L terms in creating a higher stiffness ratio. It is also interesting that the optimizer favored points close to most vertices, demonstrating the importance of constraints 3 through 6. The solution is nearly symmetrical, suggesting a more stable overall structure. The stiffness ratios for each panel were on the order of 10:1 between the non-bisection and bisection axes, showing that this panel design is viable for achieving rigid foldability while retaining the required overall stiffness when deployed.

2.5.3 Z Design

The solution found by the optimizer for a single panel of the Z design was as expected: the bisection line was only intersected by one of the support beams, while all three beams intersected the non-bisection line, increasing the stiffness in that direction. Additionally, the beam that touches the bisection line is nearly parallel to it, minimizing the intersection angle, and the others are nearly all perpendicular to the other diagonal (see Fig. 2.10). The L values seem less significant to the optimization than the angle and the intersection ratio.

The hinge points clustering around the vertices were not as predictable in this design, as some vertices have only one hinge point nearby, and others have three. The results were also not symmetric, which was unanticipated, and in particular, the geometry close to the degree-six vertex is not intuitive.

The middle segment of the Z is treated similar to a torsion bar, which helps with flexing, though because it did not take torsion into consideration, it would likely have an even higher stiffness ratio (i.e. able to flex even more along the bisection line). With that considered, the Z design without taking torsion into account had an average ratio of about 20:1. This design, therefore, is also a good candidate for the structure, depending on the flexibility needed within the panels.

2.5.4 Summary and Future Work

Using the simply supported beam model, this work was able to develop designs for the frame of a Flasher origami pattern that helps address rigid-foldability complications, allowing for a variety of panel flexibility needs. Fig. 2.12 shows a representation of how a fully optimized Flasher pattern would look for each design, with an optimized gore rotationally mirrored about the central polygon, though further experimentation and prototyping could validate whether this satisfies the rigid-foldability condition for the full Flasher. Fig. 2.13 shows a 3D printed prototype

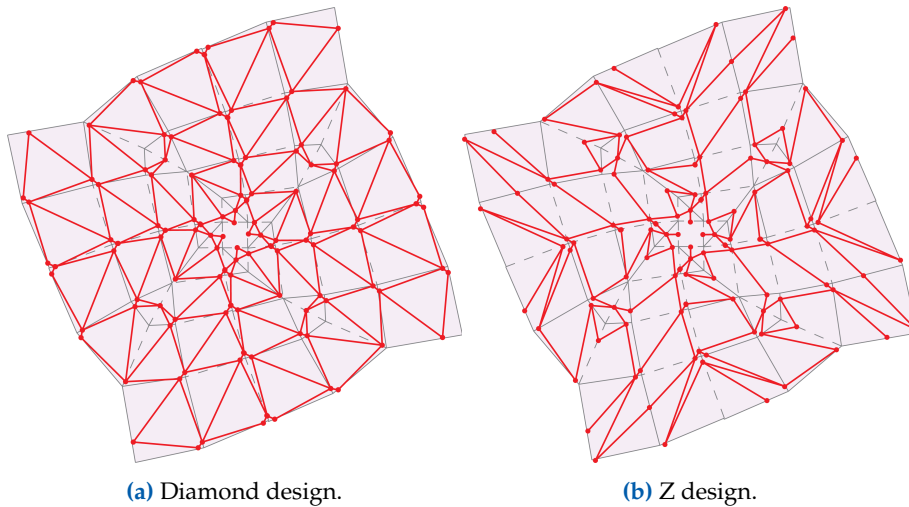


Figure 2.12: Full Flasher optimization shown overlaid with original pattern.

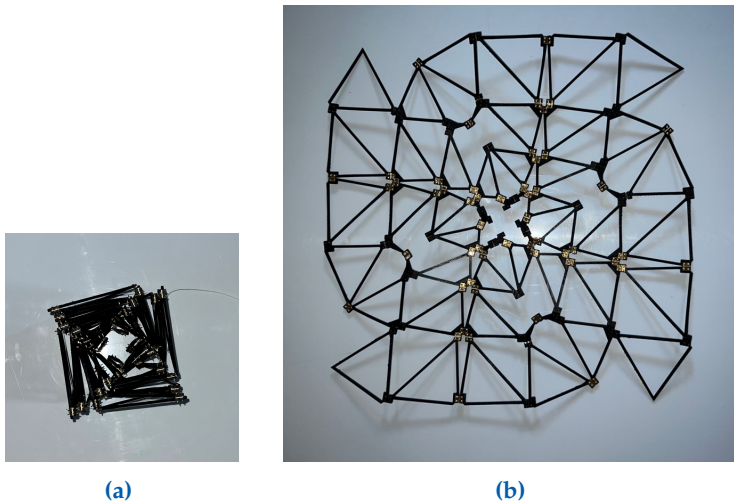


Figure 2.13: Prototype of the optimized diamond design. (a) Stowed. (b) Deployed.

of the diamond design with rigid hinges in the stowed and deployed configurations.

Future work could benefit from using a “mix-and-match” approach to the optimization of the Flasher by allowing the optimizer to choose which frame design is used on a panel-by-panel basis, rather than using the same frame design for every panel. In this way the optimization could accommodate the different requirements for each Flasher panel; for example, panels on the outer edge are larger, and would therefore require more compliance along their bisection lines to fold, as well as requiring more stiffness along the non-bisection lines to support the Flasher structure when deployed.

Additional future work recommended would be to validate the full Flasher optimization results using finite element analysis such as ANSYS, or other beam models. Prototyping of these designs is in work at BYU, but has not yet been completed.

2.6 Conclusion

This optimization is meant as a framework to help resolve rigid-foldable complications with the Flasher pattern, and shows the feasibility of creating a Flasher structure that has flexible panels. This work demonstrates the feasibility of creating a Flasher that can withstand the rigid-foldability issues, using either the diamond or Z designs. This optimization framework may also be applicable to other rigid-foldable origami patterns.

Designing Kirigami Patterns using the Hamiltonian Circuit Framework

3.1 Introduction

A common design process using origami begins with a zero-thickness pattern, which is then thickened from an original paper model using a thickness accommodation technique [22], as described by Bolanos et al. [23]. The same origami pattern may result in drastically different designs when incorporating different thickness accommodation patterns, which can make evaluating the final configuration of these designs more challenging. This bottom-up process results in various mechanical systems, with varying shapes, degrees of stowed volume efficiency, and deployed area efficiency, as shown in Fig. 3.1a. This work builds on a method of a top-down design using a Hamiltonian circuit framework, which allows a designer to choose a final deployed shape and aspect ratio, and then determine a corresponding kirigami pattern, as shown in Fig. 3.1b. This approach can result in a high ratio of the deployed surface area to stowed volume by incorporating the hinge-shift thickness accommodation technique [46]. This work also utilizes research done by Yang et al. [47–49] to explore the capability of the Hamiltonian circuit method to fold identical thick panels. Similar work by Yang et al. [50] and Yang et al. [51] has explored the design of single degree-of-freedom systems using the Hamiltonian circuit methodology. This chapter is based on work with McKaelin Edralin, Spencer P. Magleby, Denise Halverson, Zhong You, and Larry L. Howell, which is in review for publication in the 2024 International Conference on Reconfigurable Mechanisms and Robots (ReMAR) [24].

Figure 3.1 shows an overview of how the bottom-up and top-down design methods works. It should be especially noted how the bottom-up method results in various deployed shapes which may or may not align with the origami pattern shape originally chosen by the designer. In contrast, the top-down method allows a kirigami pattern to be created for a final shape which can be precisely known beforehand and can align closely with the desired deployed shape chosen by the designer.

The top-down method allows designers the ability to tailor a shape to their specific needs and use-case more easily than the bottom-up method. It also incorporates a simple thickness accommodation method which results in 75% to 100% stowed volume efficiency, depending on

[22] Lang et al., “A review of thickness-accommodation techniques in origami-inspired engineering,” 2018.

[23] Bolanos et al., *A Preliminary Approach to Select an Origami Source Pattern for Deployable Space Arrays*, 2022.

[46] Lang et al., “A Review of Thickness-Accommodation Techniques in Origami-Inspired Engineering,” 2018.

[47] Yang et al., “Folding and deploying identical thick panels with spring-loaded hinges,” 2022.

[48] Yang et al., “Data for “Folding and Deploying Identical Thick Panels with Spring-loaded Hinges,”” 2022.

[49] Yang et al., *Compactly Folding Rigid Panels With Uniform Thickness Through Origami and Kirigami*, 2019.

[50] Yang et al., “Design of Single Degree-of-Freedom Triangular Resch Patterns with Thick-panel Origami,” 2022.

[51] Yang et al., “Folding arrays of uniform-thickness panels to compact bundles with a single degree of freedom,” 2022.

[24] Coleman et al., *A Methodology for Designing and Improving Novel Kirigami Patterns using the Hamiltonian Circuit Framework (In-Review)*, 2024.

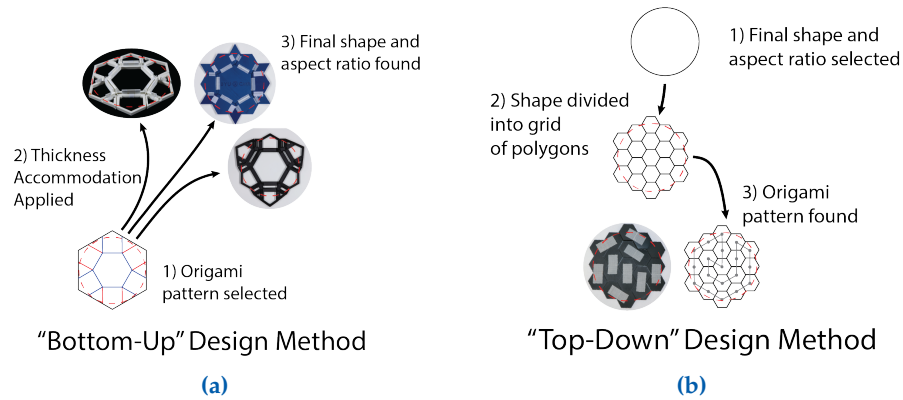


Figure 3.1: Comparison between the final designs created using the bottom-up and top-down design methodologies. (a) Bottom-Up design methodology. (b) Top-Down design methodology.

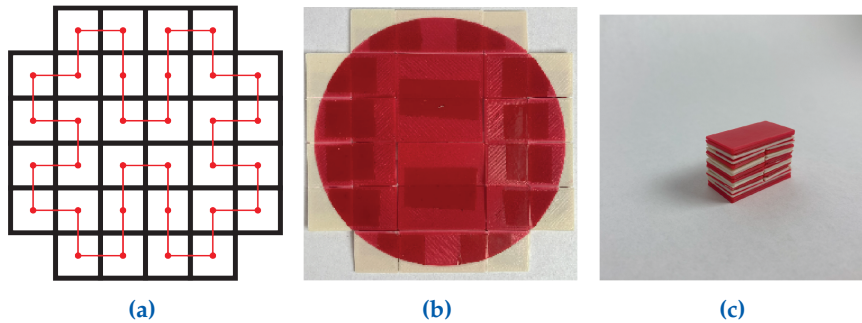


Figure 3.2: Example of how a Hamiltonian circuit can be used to create a compactly stowing array which deploys out to a large area. (a) Circuit imposed on a square grid. (b) 3D printed prototype created from circuit, shown in deployed state. Note that the circle shown in the middle of the pattern is representative of the effective RF area of this pattern. Other patterns shown in later sections will also be shown with their effective RF areas for comparison. (c) 3D printed prototype created from circuit, shown in stowed state.

the polygon chosen for the base grid. An example of a pattern created with a square-based grid is shown in Fig. 3.2, with its associated folding states shown in Fig. 3.3.

In this paper, methods will be reviewed which have been developed by various authors to create kirigami patterns using Hamiltonian circuits, discuss techniques for modifying and improving the behavior and performance of kirigami patterns created using the Hamiltonian circuit method, and then show an example implementation of this method for creating unique patterns for a particular application.

3.2 Background

The basis of creating a Hamiltonian circuit was first described by the mathematician William Rowan Hamilton in 1843 when he discovered the system of quaternions during his effort to extend complex numbers to three-dimensional space [52]. A Hamiltonian circuit (sometimes referred to as a Hamiltonian path or chain), is a concept used in graph theory

[52] Hamilton, *The Mathematical Papers of Sir William Rowan Hamilton*, 2006.

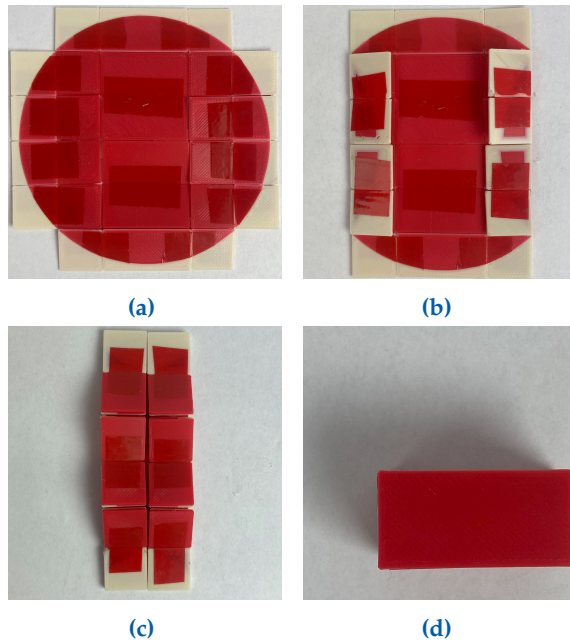


Figure 3.3: Example folding sequence for a kirigami pattern created using this methodology.

which connects a series of adjacent points by starting and ending on the same point and visiting each point exactly one time. This concept has been used in computer science applications which deal with multiple potential solutions, such as planning routes, scheduling tasks, and designing optimal computational sequences. However, for many of these applications the Hamiltonian circuit method is non-ideal as finding all possible Hamiltonian circuits is NP-complete, meaning that it may be impossible to solve in polynomial time. The use of Hamiltonian circuits for creating folding patterns in kirigami designs was proposed by Yang et al. [49] for the application of folding rigid panels with uniform thickness. They demonstrated the ability of Hamiltonian circuits to help in the design of the placement of revolute joints throughout a grid of uniform polygons, such that the grid could be folded up and stowed compactly.

The general method of using Hamiltonian circuits to design a kirigami folding pattern is as follows:

1. The designer begins with a tiling of the plane by regular polygons, which represent a deployed pattern of individual uniform panels. A bounded subset of this tiling is referred to as a “grid”.
2. A desired deployed shape is chosen and imposed on the grid, leaving only the panels required to create the shape.
3. If possible, a simple closed loop is found consisting of line segments, having endpoints at the center of adjacent tiles and which connects all the tiles^a [53].

[49] Yang et al., *Compactly Folding Rigid Panels With Uniform Thickness Through Origami and Kirigami*, 2019.

^aNP-complete problems have not been proven to be able to be solved in polynomial time, leading to the impossibility of assuring that any solution may exist. This is referred to as the P vs NP problem in mathematics, and is one of the famous unsolved problems in mathematics. Additionally, because a pattern may consist of any combination of arbitrary shapes, there may exist some patterns for which a closed circuit is not guaranteed to be possible.

[53] Institute, “P vs NP,” 2023.

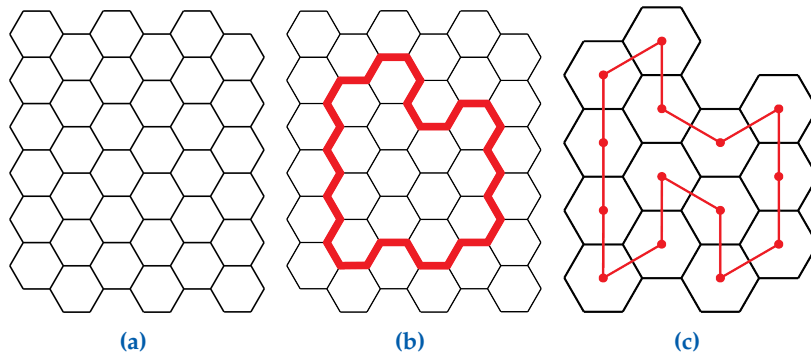


Figure 3.4: Example kirigami pattern selection using Hamiltonian circuits. Note that an unusual pattern was chosen to illustrate how a circuit may consist of an arbitrary group of grid cells. (a) Initial grid of hexagons. (b) Final deployed shape drawn onto grid. (c) Hamiltonian circuit drawn onto extracted shape.

4. This circuit is then used to determine cut and fold locations within the pattern. This process is shown in Fig. 3.4 as applied to producing an arbitrary pattern.

This method has the ability to produce unique, unconstrained, and versatile resulting shapes. Determining the folding sequence for the chosen pattern is more difficult and will be detailed hereafter.

A major consideration when creating a pattern is that the pattern should contain an even number of panels. This is because the folding is dependent on a sequence of mountain-valley folds, and patterns with an odd number of panels would result in folds that did not align at the ends of the circuit. Methods for developing patterns with an odd number of panels are discussed in Section 3.4.1. Further considerations for choosing a base grid and resulting pattern will be discussed throughout this work.

It should be noted that combinations of varying polygons may also be used, although it is generally more complicated to illustrate; however, a pattern using both squares and triangles will be shown in Section 3.5.

3.3 Creating Folding Patterns

Given an arbitrary set of points, a Hamiltonian circuit is a closed path which connects all points and visits each point once. Creating a Hamiltonian circuit is an NP-complex problem, and no valid solution is guaranteed for an arbitrary set of points. However, by constraining the points to a predetermined grid of identical polygons, the number of solutions increases, even becoming exponentially related to the number of panels in the chosen pattern, or N . Extensive experimentation suggests that the pattern created will also have a number of folding groups proportional to the number of sides on the polygon chosen, or n , meaning that patterns based on triangles will have three unique folding groups, patterns based on squares will have four unique folding groups, patterns based on hexagons will have six unique folding groups, and so on. These factors combine to create a large design space to work with, as any unique

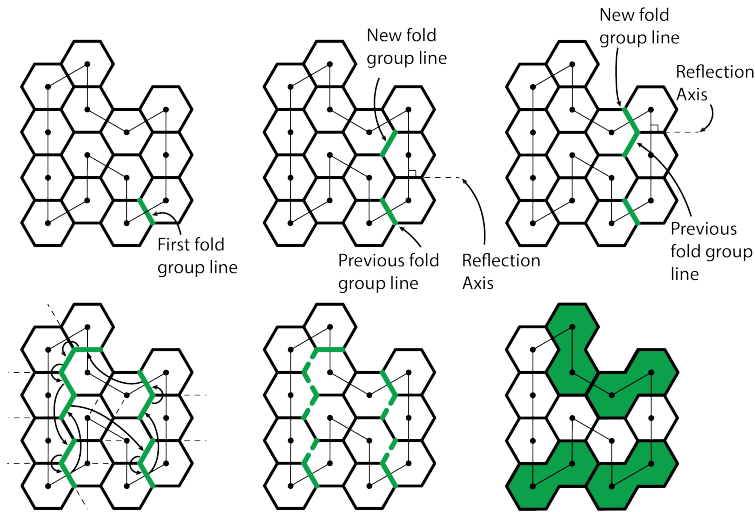


Figure 3.5: Reflection sequence used to find valid fold groups. Fold group lines that do not cross the Hamiltonian circuit and will therefore not be used for folding are shown as dashed.

pattern will generally have multiple viable circuits, and each circuit will have n possible folding sets.

Each folding set will result in a double stack with a pair of panels on the top and a pair of panels on the bottom, and all other panels folded in between these two pairs, as shown in the stowed pattern in Fig. 3.2c. These pairs on the top and bottom are referred to as duplets. Finding possible top and bottom pairs is a necessary, but not sufficient, condition for foldability.

To find valid folding sequences for the Hamiltonian circuit found, the Hamiltonian circuit found is used to determine which lines in the pattern chosen will be folded and which lines will be cut. When the circuit is superimposed on the pattern, pattern lines which intersect with the circuit path line will become folded, whereas lines on the pattern which do not intersect with the circuit path will be cut. Finding the fold lines first where to begin looking for a new folding group.

The first folding group is found by defining an initial fold group line. This line is may be any of the pattern lines which intersects the Hamiltonian circuit chosen. A reflection line is then defined as the next pattern line which is intersected by the circuit. The initial fold line is then reflected over the reflection line to find the next line in the fold group associated with the initial fold group line. This process is then repeated until the reflected line returns back to the initial fold line on the pattern, as shown in Fig. 3.5.

The initial folding group shown in Fig. 3.5 demonstrates that some lines found during this process intersect with the circuit found and will become folding lines, and other lines found do not intersect with the circuit and therefore have no impact on the final folding sequence. Because all pattern lines which do not intersect with the circuit will be cut, the lines found in each folding group which do not intersect with

the pattern can be disregarded.

The fold lines which do intersect the circuit can be seen to fall between two adjacent panels, and as such each line left in the group defines a set of panels in that group, referred to here as a duplet. These duplets are then used as the top or bottom pair of panels in a folded circuit. The reflection process used allows duplets to be found which will be aligned with each other in the folded state; attempts to fold the pattern using top and bottom duplets which are not contained in the same fold group will result in the top and bottom being rotationally misaligned, precluding the possibility of folding with rigid panels. While this process allows for the verification of alignment between top and bottom pair of duplets within the circuit for folding, it gives no information about the folding sequence required to stow the pattern and more work is required to verify that the resulting pattern may fold.

This process is then repeated for each folding line in the pattern, although folding lines which have been included in previous groups may be skipped as they will yield the same folding group which was previously found. At the end of this process, there are 1 or more lines in each folding group which intersect with the pattern and will become folding lines in that group.

This process allows for the categorization each folding line into one of n groups, where n is the number of sides on the base polygon of the pattern. Fig. 3.6a shows the folding groups that result from this process for the pattern shown, there being 6 total as the base polygon is hexagonal. Note that each color in Fig. 3.6 represents a unique folding group. Once all folding groups have been found, folding sequences may be chosen from the folding groups which contain at least two folding lines. At least 2 folding lines are required in a group for the pattern to be able to be stowed, because each folding line found in the group defines a duplet which must be aligned with another duplet defined by the other folding lines in the group to fold correctly. This method of stowing patterns requires that there be a duplet on both the top and on the bottom of the stowed pattern, as shown in the example in Fig. 3.2c. Groups with less than two folding lines will be lacking a duplet which may align on the top or bottom when stowed. Fig. 3.6b shows how at the end of this process, the pattern-circuit combination may be characterized by the folding groups found. It may be noted that some folding groups may have three or more folding lines and corresponding duplets in a group. In these cases, any two folding lines may be chosen, and their respective duplets will align as top or bottom pairs. Note that two groups shown in Fig. 3.6, purple and yellow, have only one duplet in their group, meaning that they will not result in a valid folding sequence. When using patterns based on square grids, the same method is used; however, a simplified method for finding duplets can be used. This is explained and shown in Appendix A. To compactly stow a pattern with the highest stowage efficiency, a folded pattern should have an equal number of panels in between the pair of duplets chosen as top and bottom pairs. This is simple to determine, as the number of panels between each pair

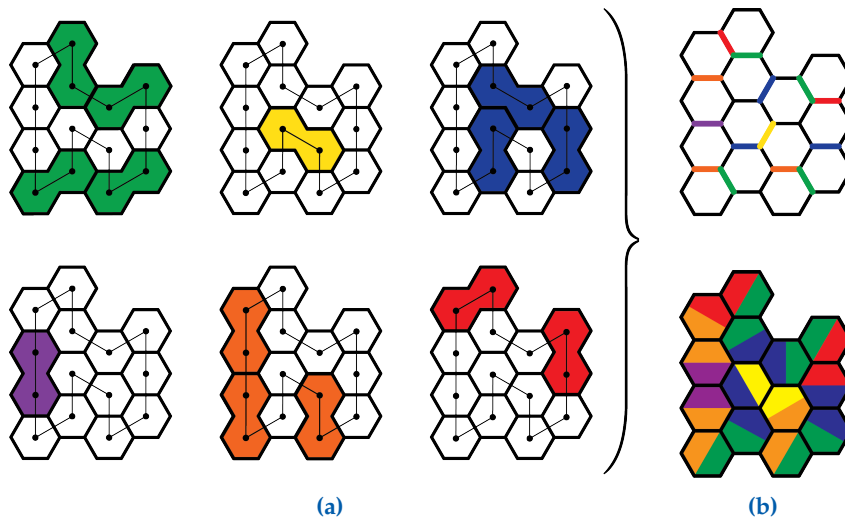


Figure 3.6: Fold groups created from unique pattern-circuit combination. All duplets of hexagons with identical colors are valid folding combinations with any other duplet of the same color. (a) Fold groups for selected kirigami pattern. Note that because the principal polygon was six sided, there are six unique fold groups. (b) All valid folding groups for selected kirigami pattern.

of duplets can be counted, and a pair of duplets with an equal number of panels between them can be favored. In the case illustrated in Fig. 3.6b, the combination given by the top blue duplet and the leftmost blue duplet is the only valid pair of duplets which meets this criteria and would result in a perfectly compact stowed pattern. Other considerations will be discussed in Section 3.5 and will be shown applied to specific patterns.

3.4 Additional Techniques

There are several additional techniques which can be used to modify the performance and behavior of patterns designed using Hamiltonian circuits. These include tessellation, merging panels, and incorporating open loops. Moreover, additional techniques are sure to be discovered when applied to new uses.

3.4.1 Merging Panels and Incorporating Open Chains

One of the main drawbacks to the design of patterns using the Hamiltonian circuit methodology is that the resulting patterns consist of long kinematic chains with many degrees-of-freedom. This can be mitigated by merging panels which experience concurrent motion in the folding sequence, as shown in the example in Fig. 3.9a. Merging panels consists of removing the cut line between two panels, such that they are united into a single panel. The effect of merging panels can be directly calculated using the Chebychev–Grübler–Kutzbach criterion, which can be used to find the mobility of both simple open and simple closed chains. The

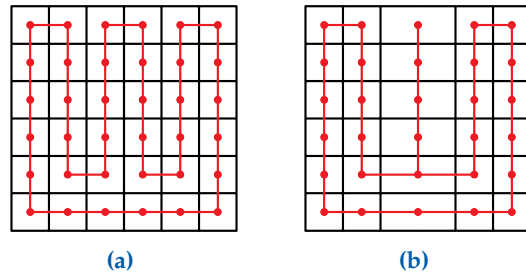


Figure 3.7: (a) Square-based pattern with 36-panels connected with a single closed loop. (b) Updated pattern after merging panels consisting of a closed loop and an open loop.

mobility of a simple open chain is given by

$$M = \sum_{i=1}^j f_i \quad (3.1)$$

and the mobility of a simple closed chain is given by

$$M = \sum_{i=1}^j f_i - 6 \quad (3.2)$$

where M is the degrees-of-freedom of the system, j is the number of joints, and f_i is the freedom of each joint.

Merging panels should occur in every pattern in the top and bottom pair of duplets that define the circuit, as neither panel in a duplet is moving relative to the other. The example in Fig. 3.7 shows the difference that merging multiple panels can make to the mobility of the system. In Fig. 3.7a, the circuit imposed on the 36-panel square pattern results in a mobility of $M = 30$, which is calculated using Equation 3.2 for a single closed chain. As panels are merged, however, the circuit becomes an closed chain connected to an open chain. Fig. 3.7b shows this, and the resulting mobility can be calculated as $M = 24$, found by using both Equations 3.1 and 3.2 for each corresponding section of the new circuit. The effect of the creation of open chains while merging panels was originally noted by Yang et al. [47], and merging panels generally results in lowering the overall complexity of the system despite the open chains it creates.

[47] Yang et al., "Folding and deploying identical thick panels with spring-loaded hinges," 2022.

Incorporating open chains can also be useful for accommodating and enabling geometry which may not otherwise be able to fold as a closed circuit. Single closed-chain patterns may be impossible for a given grid due to a variety of reasons, such as having an odd number of panels or an even number of panels containing no pair of duplets within a folding set. Nesting combinations of both open and closed chains allows for creation of deployed geometries which are otherwise impossible. To accommodate this geometry, panels can be removed to produce a pattern with an even number of panels, which is then used to find a valid folding pattern. Once this pattern is found, the removed panels can be added

back to the pattern as an open chain, as long as it is connected to one of the top or bottom duplets. This results in a closed chain with $n - r$ panels and an open chain with $r + 1$ panels, where r is the number of panels which have been removed. An example of this is apparent in hexagonal patterns with a circular shape, such as those shown in Section 3.5.4 and Section 3.5.5.

3.5 Applications in Patterns with Potential for Deployable Radio Frequency Arrays

The design space associated with the Hamiltonian circuit methodology is large; however, when additional constraints are applied the design space shrinks considerably. In this section, patterns are considered which can be used for large (5-10 meter diameter), space-based radio frequency (RF) antennas, although other applications may result in differing ideal geometries, such as for SmallSat applications or arrays used primarily to generate solar power. Some constraints presented in this section are manufacturability, practicality, and RF applications. Practicality takes into account the total number of panels and degrees-of-freedom in the system. Because applications for RF antennas are considered in this work, deployed areas closer to that of an inscribed circle were viewed as more ideal. Although every application is unique, large antenna applications are considered in this work and made the assumption that the largest panel would be on the scale of roughly 1 meter, and as such sought to maintain a roughly 1:5-1:10 ratio between the width of one panel and the width of the entire array. Another consideration that was used throughout was that the pattern should maximize volume efficiency by having an even number of panels on each side of the stowed pattern, as explained in Section 3.2.

With each of these considerations in mind, the design space shrinks appreciably, and 5 patterns were created to satisfy these requirements and are viable candidates for future work on large space-based antenna designs. While five patterns will be considered and compared, it can be noted that there are many other possible candidates that could be created using this methodology to satisfy the requirements, with varying behavior, stowed volume efficiency, and deployed area efficiency. These 5 patterns were chosen because they all have an aspect ratio of about 1, making them ideal baseline patterns for future comparison. Trade-offs for each option will be discussed. These designs use both square panel and hexagonal uniform panels. The overview of each pattern with its accompanying parameters can be seen in Fig. 3.8, which also includes a scale comparison of the circumscribed circle area of the each deployed pattern, and a scale comparison of the stowed side and top area of each pattern, with associated parameters. Note that the 32-panel square pattern shown in Fig. 3.8c also uses equilateral triangles on each corner in addition to the primarily square grid. To compare each pattern, calculations were kept non-dimensional, considering a unit panel with a length of a .

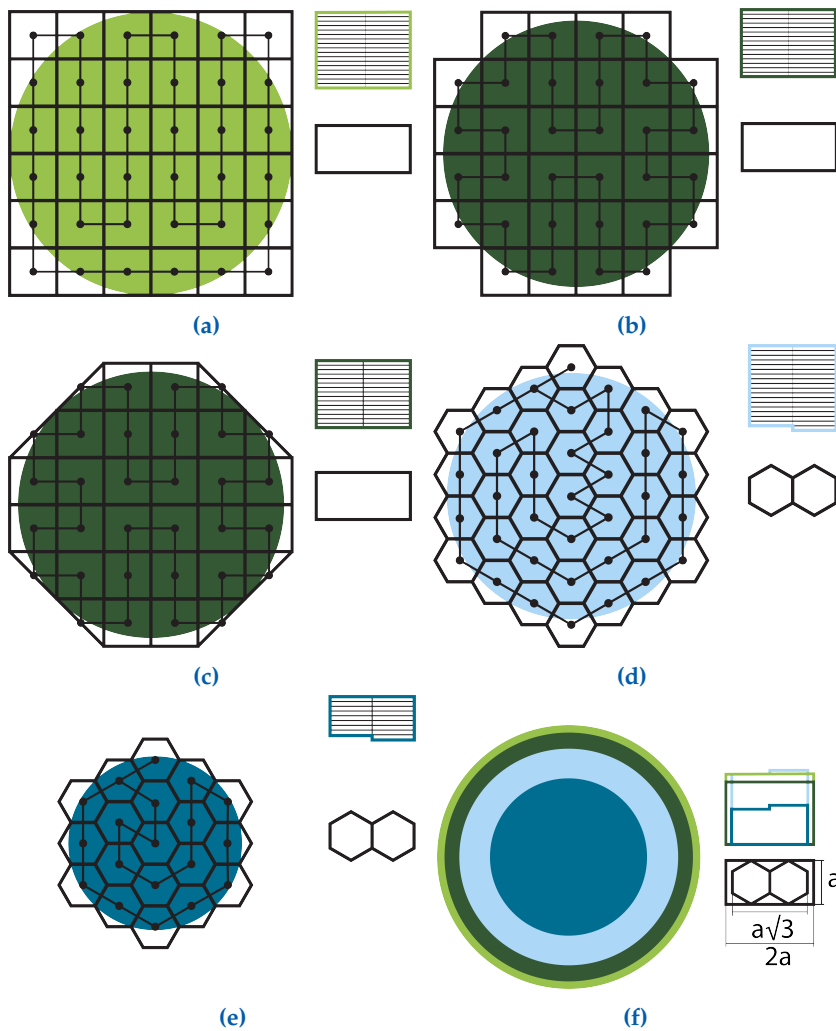


Figure 3.8: Explored patterns with example Hamiltonian circuits superimposed on top of each. Details of each pattern are given in Table 3.1. (a) 36-panel square pattern. (b) 32-panel square pattern. (c) Quasi-Octagon pattern. (d) 37-panel hexagonal pattern. (e) 19-panel hexagonal pattern. (f) Scale comparison of the circumscribed circle area of the each deployed pattern on the left, and a scale comparison of the stowed side and top area of each pattern on the right, with associated parameters. Dark blue corresponds with the 19-panel hexagonal pattern, light blue corresponds with the 37-panel hexagonal pattern, dark green corresponds with the Quasi-Octagon and 32-panel square patterns, and light green corresponds with the 36-panel square pattern.

3.5.1 36-Panel Square Pattern

The 36-panel square pattern, shown in Fig. 3.8a, is the result of the most basic design from the requirements. It is intuitive and simple to draw. Additionally, there are a plethora of viable Hamiltonian circuits that may be created with this grid, including many that result in reduced degrees-of-freedom from the merging of panels which have identical kinematics. This pattern results in the highest overall area of all the patterns considered; however, it results in a significant amount of area which is unused in RF applications on each corner.

3.5.2 32-Panel Square Pattern

In exploring the 36-panel square pattern, it was found that by reducing the diameter of the inscribed circle slightly, the four corner panels could be removed, as shown in Fig. 3.8b. This results in an 11.76% decrease in total RF area, with an identical 11.76% decrease in the total mass and stowed volume of the antenna. This configuration is preferable to the 36-panel square pattern when mass and stowed volume are prioritized over pure performance. This design also consists solely of square panels, simplifying manufacturing and the incorporation of existing components.

3.5.3 Quasi-Octagon Square Pattern

The benefits of the 32-panel square pattern in mass reduction can be further improved by cutting off the outer halves of the corner panels, as shown in Fig. 3.8c. This results in a 25% decrease in total mass as compared to the 36-panel square pattern, while retaining the same 11.76% decrease in total usable RF area. This pattern maintains the same stowed volume as the previous 32-panel square pattern and increases the number of unique panels, but it would be preferable when mass must be minimized as much as possible.

It should be noted that in continuing the pattern of optimization for reduced mass, all excess which did not conform to the circumscribed circle could be removed. However, as shown with the Quasi-Octagon pattern, the stowed volume remains the same because the number of panels and corresponding thickness when stowed is unchanged, and the mass gains from further material removal would be minimal, decreasing at most by 10.24% while increasing the manufacturing complexity of the pattern by several unique panels. Additionally, a similar pattern could be formed by using smaller and smaller panels, allowing for more panels to be removed from each corner as to increase the area efficiency of the design, but such a design would be increasingly impractical, as the number of panels required would increase exponentially. As such, the Quasi-Octagon pattern is considered in this work to be the most optimal version of minimizing mass, maximizing RF area, and maintaining practicality for the purposes of manufacturability and deployment by modifying the initial panel shape.

3.5.4 19-Panel Hexagonal Pattern

When considering the RF requirement that the deployed area would be evaluated on its conformance to a circular shape, patterns based on hexagonal grids were a natural solution. Two patterns based on hexagons were explored, one with 19-panels, shown in Fig. 3.8e, and one with 37-panels, shown in Fig. 3.8d.

By using a grid of hexagons, which are by their nature more circular than squares, the 19-panel pattern is able to achieve a used area efficiency 82.74%, a 5.21% increase from the 36-panel square and 32-panel square patterns. This pattern has a significantly smaller overall area than other patterns, but this is due to the use of a unit cell measurement, and as

such, other metrics, such as deployed area efficiency and stowed volume efficiency may be considered more useful for comparison purposes.

The 19-panel hexagonal pattern also shows an interesting consideration when using hexagonal patterns with an aspect ratio of 1, which is that such patterns have an odd number of panels which are unable to evenly stack in two piles. Because of this, one panel is removed from the pattern when determining Hamiltonian circuits, using the method described in Section 3.4.1.

3.5.5 37-Panel Hexagon Pattern

The 37-panel hexagon pattern takes the benefits of the 19-panel hexagon pattern and increases the relative RF area by adding an order to the outside of the pattern, which is shown in Fig. 3.8d. Implementing the technique of trimming panel shapes to reduce the mass of the system and maintain the viable RF area as shown with the Quasi-Octagon pattern was considered, and it was found that removing the outer half of the most unused hexagons would increase the area efficiency of the pattern by 7.21% to a total of 88.91% while only increasing the complexity by one unique panel. This would result in a very good used area efficiency, second only to the Quasi-Octagon pattern. However, this idea was overshadowed by the fact that hexagonal patterns are much more complex to fold, and the kinematics of which are difficult to predict and simplify. In fact, in exploring many hexagon based patterns, very few were found to have any folding sequences that could be simplified through the merging of panels, and these patterns were often subject to a unique series of steps involving non-adjacent panels, making it very difficult to predict valid deployment sequences. These factors negate the benefits of compact stowage, in that they would generally require complex deployment mechanisms to be incorporated into the design. Because of this, hexagonal patterns were not explored further, and it is put forward that for the application of this section, they are not ideal candidates for deployable arrays which are low-mass, high-area, and practical.

3.5.6 Comparison of Potential Patterns

When considering which pattern may be the best fit for a given application, it is appropriate to compare the patterns based on a variety of criteria. Deployed area and stowed volume are often used as the most basic criteria for deployable space-based applications, and variations of these are used in this work. Additionally, prototypes from various patterns were tested and results will be discussed, although not all models will be shown in this work.

Various advantages and disadvantages of each pattern have been discussed and will be used to make determinations about the feasibility and attractiveness of each design. A general theme that was found was that patterns based on a square grid are more likely to be able to be simplified by finding methods of concurrent deployment between differ-

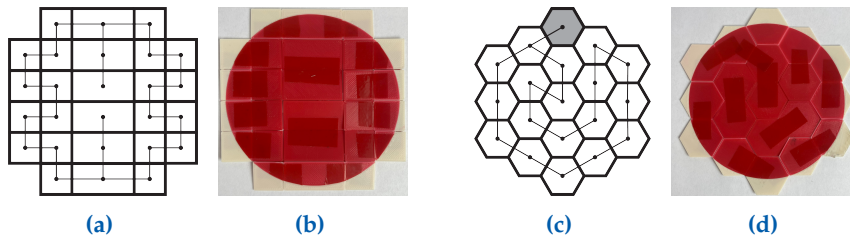


Figure 3.9: Example implementation. (a) Valid Hamiltonian circuit for 32-panel square grid. (b) 3D printed prototype showing example of merged panels to reduce the overall degrees-of-freedom. (c) Valid Hamiltonian circuit for 19-panel hexagonal grid. Note that because the grid has an odd number of panels, one panel must be connected by a separate circuit on the back, shown in gray. (d) 3D printed prototype.

ent panels to reduce the degrees-of-freedom of the system. Contrarily, patterns based on hexagonal grids resulted in complicated kinematics which are non-trivial and are rarely, if ever, able to be simplified. An example prototype of the 32-panel square pattern is shown in Fig. 3.9b, with its corresponding Hamiltonian circuit shown in Fig. 3.9a. This prototype shows an example of a simplified pattern, with the vertically middle two columns shown with “merged” panels. An example of the 19-panel hexagonal pattern is shown in Fig. 3.9d, with its corresponding Hamiltonian circuit shown in Fig. 3.9c.

In general, this makes square-based patterns more compelling candidates for design than their hexagonal counterparts. This is especially highlighted by the Quasi-Octagon design, which incorporates the simplicity of the square grid with an area efficiency exceeding that of the hexagonal grids explored. Because the primary motivation and advantage of the hexagonal based patterns was their area efficiency, which was superior when compared to the 36 and 32-panel square patterns, this advantage in the Quasi-Octagon pattern suggests that patterns based on hexagonal grids are not ideal for the purposes of designing simple, large, space-based deployable arrays at this time. Even if there were significant stowed volume or deployed area efficiency advantages with hexagonal patterns, the complicated nature of the resulting kinematics alone would be enough to give any designer pause. One of the aims of this work was to explore patterns based on Hamiltonian circuits and justify why some patterns are more suitable than others for the intended applications. Patterns based on hexagons are more complicated, unconstrained, and unpredictable than patterns based on squares, and there exist other options which have the same benefits and are more ideal for the applications discussed.

One method of determining which design is the best for a given application is to use a weighted ranking method based on relevant design parameters and characteristics, such as stowed volume, total mass, and deployed area efficiency. A summary of relevant characteristics for the patterns discussed is given in Table 3.1. An example of a weighted ranking system approach to determining which pattern is best suited to the given use case is shown in Table 3.2. In this example, the best pattern

for each major parameter received 2 points, the second best received 1 point, and the worst received -1 point. While this simple example has limitations, it is sufficient to illustrate the method. In this example, it can be seen that several patterns, such as the 36 and 32-panel square patterns, are the best in some categories (deployed area and volume efficiency) but are the worst in deployed area efficiency. The best pattern overall was found to be the Quasi-Octagon, as it combines the best volume efficiency of the square patterns with the best area efficiency. Another way to further examine various patterns would be to apply a weight to each individual parameter, such as if volume efficiency is more important than deployed area efficiency, and future designers would be wise to consider their needs when making a decision as to which pattern is best suited to their application.

3.6 Future Work

One of the initial considerations used in this work when exploring potential patterns was that each stack in the stowed patterns should have the same number of panels. While this simplifies the stowed volume, it is not strictly necessary. One of the major benefits of using Hamiltonian circuits is that they have a simple thickness accommodation built-in, meaning that thick panels do not complicate the pattern implementation. This means that patterns which have an unequal number of panels in each stack could be utilized in other ways, such as selectively thickening panels in the stack with fewer panels, and incorporating electronics or other components into the thickened panels. This has the potential of increasing the volume efficiency of the entire satellite system as a whole, rather than just considering the antenna alone. Ideally, every component in the satellite could be incorporated into a thick panel with RF on the outside, and the entire system could fold compactly and deploy as one

Table 3.1: Summary of Pattern Tradeoffs

Metric	36 Panel, Square	32 Panel, Square	Quasi-Octagon	19 Panel, Hexagonal	37 Panel, Hexagonal
Number of Panels	36	32	32	19	37
Degrees-of-Freedom	29	25	25	19	37
A_{panel}	a^2	a^2	$a^2 \text{ and } \frac{1}{2} a^2$	$\frac{3\sqrt{3}}{8} a^2$	$\frac{3\sqrt{3}}{8} a^2$
A_{total}	$36a^2$	$32a^2$	$28a^2$	$\frac{57\sqrt{3}}{8} a^2 \approx 12.34a^2$	$\frac{111\sqrt{3}}{8} a^2 \approx 24.03a^2$
$r_{circumscribed}$	$3a$	$2a\sqrt{2}$	$2a\sqrt{2}$	$\frac{\sqrt{52}}{4} a$	$\frac{\sqrt{5}}{2} a$
A_{RF}	$9\pi a^2$	$8\pi a^2$	$8\pi a^2$	$\frac{52}{16}\pi a^2$	$\frac{25}{4}\pi a^2$
$A_{RF}(\#)$	28.27	25.13	25.13	10.21	19.64
η_A	$\frac{\pi}{4} \approx 78.54\%$	$\frac{\pi}{4} \approx 78.54\%$	$\frac{2\pi}{7} \approx 89.76\%$	$\frac{26\pi}{57\sqrt{3}} \approx 82.74\%$	$\frac{50\pi}{111\sqrt{3}} \approx 81.70\%$
Thickness stacked	$18t$	$16t$	$16t$	$10t$	$19t$
Length	$2a$	$2a$	$2a$	$a\sqrt{3}$	$a\sqrt{3}$
V_{stowed}	$36ta^2$	$32ta^2$	$32ta^2$	$10\sqrt{3}ta^2 \approx 17.3ta^2$	$19\sqrt{3}ta^2 \approx 32.9ta^2$
η_V	$\frac{\pi}{4} \approx 78.54\%$	$\frac{\pi}{4} \approx 78.54\%$	$\frac{\pi}{4} \approx 78.54\%$	$\frac{52\pi}{160\sqrt{3}} \approx 58.95\%$	$\frac{25\pi}{76\sqrt{3}} \approx 59.66\%$
η_{cuboid}	100%	100%	100%	75%	75%
η_{panel}	3.54%	3.98%	3.98%	6.36%	3.31%

unit. Each stowed pattern resulted in a shape that was twice the size of each individual panel. Future work could also modify this, and create a pattern using a grid of “half-squares” or “half-hexagons”, such that the final stowed shape was a single unit. This would be functionally the same process of design, and would result in twice as many panels and degrees-of-freedom, but could result in compact geometries for specific applications.

This work was also limited to the study of single antenna applications. Another interesting benefit of patterns based on Hamiltonian circuits is that they may be easily tessellated. Future work may benefit from exploring patterns which are especially designed to be tessellated once deployed in space.

3.7 Conclusion

The design space created by Hamiltonian circuits as an origin for creating kirigami patterns yields innovative results and has immense potential for unique deployable applications. The designs that result from this methodology have simple thickness accommodation, high stowage efficiency, and predictable deployed area efficiency. This makes them prime candidates for future exploration and implementation, which is certain to give promising results and functional designs.

Table 3.2: Example weighted ranking method for determining preferred pattern

Metric	36 Panel, Square	32 Panel, Square	Quasi-Octagon	19 Panel, Hexagonal	37 Panel, Hexagonal
$V_{circumscribed}$	3	2.828	2.828	1.803	2.5
A_{RF}	28.27	25.13	25.13	10.21	19.64
η_A	78.54	78.54	89.76	82.74	81.70
Thickness stacked	18	16	16	10	19
Length	2	2	2	1.732	1.732
V_{stowed}	36	32	32	17.3	32.9
η_V	78.54	78.54	78.54	58.95	59.66
η_{cuboid}	100	100	100	75	75
η_{panel}	3.54	3.98	3.98	6.36	3.31
Best (2)	2	1	2	1	0
Second best (1)	0	2	2	1	0
Worst (-1)	1	1	0	2	2
Score	3	3	6	1	-2

4

Modeling and Analysis of Slipping in Rolled Gossamer Arrays

4.1 Introduction

Inspired by the precision requirements of reflectarray antennae, this research focuses on gossamer arrays that reduce the wrinkling that commonly occurs in stowed membranes [54] by rolling sections of the array [27, 28, 55]. Gossamer structures are systems which are typically constructed from flexible membranes, which have the advantages of being lightweight, flexible, and easily stowable, such as the example shown in Fig. 4.1. Examples of gossamer structures include solar sails and sun shades. This work characterizes the relative motion in rolled gossamer arrays, proposes a model for simulating this behavior, uses the model to show trade offs and trends when changing competing design parameters, and shows an implementation of hinges that accommodate this motion. This chapter is based on work with Jake Sutton, Ivy Running, Spencer P. Magelby, and Larry L. Howell, which is in review for publication in the 48th Mechanisms and Robotics Conference (MR) at the International Design Engineering Technical Conferences and Computers and Information in Engineering Conference (IDETC-CIE) [32].

4.2 Background

One of the main challenges of designing rolled gossamer structures is that buckling and plastic deformation occurs if slipping is not allowed between adjacent sections of the membrane. The terms “panel” and “strips” will be used interchangeably to refer to these adjacent sections. Panel slipping occurs in patterns using rolled membranes because the membrane layers on the outer part of the roll have further to travel than the inner membrane layers. Although the difference in diameter between the inner and outer layers may be small, it can have significant consequences to the alignment of the satellite elements, negatively impacting capability and performance of an otherwise impressive array. A simple example of the slippage between membrane layers can be observed by rolling up any softcover book; pages can be seen to immediately separate from each other as shown in Fig. 4.2a. However, this effect makes creases in a continuous folded membrane problematic, as they do not allow for relative motion in the direction of slippage required for rolling as the

[54] Tang *et al.*, “Space membrane wrinkle analytical model based on piecewise stress field,” 2023.

[27] Arya *et al.*, “Ultralight structures for space solar power satellites,” 2016.

[28] Fang *et al.*, “Development of a 7-meter inflatable reflectarray antenna,” 2004.

[55] Arya *et al.*, “Wrapping thick membranes with slipping folds,” 2015.

[32] Coleman *et al.*, *Modeling and Analysis of Inter-Panel Slipping for the Design of Rolled Gossamer Arrays (In-Review)*, 2024.

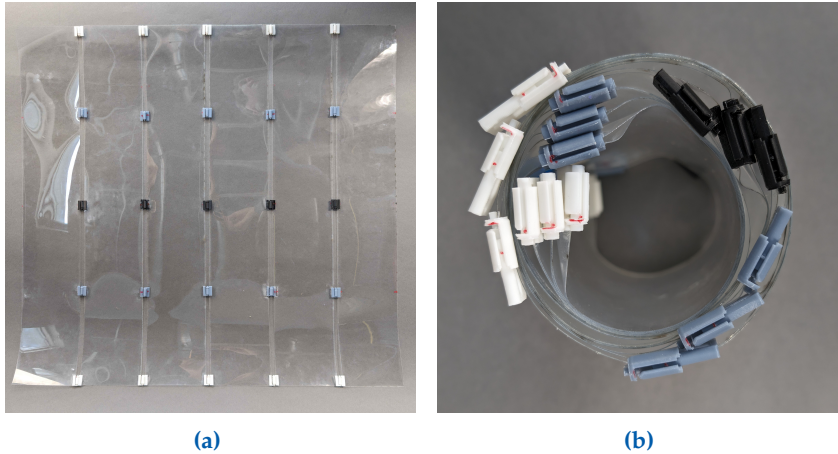


Figure 4.1: Example implementation of a gossamer pattern. (a) Deployed state, showing how a design may be visualized as a series of strips connected by hinges. In this example, there are 5 hinges connecting each set of adjacent panels. (b) Rolled state. This model is shown in the an additional possible rolled state in Fig.4.8.

pages of a book do, leading to wrinkling and deformations in the design.

This work aims to characterize the slipping motion in patterns made with parallel rectangular strips, such that slippage can be accurately predicted and accommodated. If the amount of slippage required for a given array can be known beforehand, designers can implement techniques to allow for sufficient motion and preserve the performance of the array. As such, effects of changing model parameters are shown, and trends which may be used by designers to predict behavior are illustrated.

4.3 Model

Gossamer patterns are defined by a variety of variables generally based around their required performance; these may include length and width dimensions, thickness, number of panels, surface characteristics, material properties, and so on. The method proposed predicts the amount of slippage that occurs using four of these, which are the number of panels, the thickness of each panel, the length of each panel, and the minimum bend radius of the material. A fifth variable may be included, which is how the array is rolled. Three simple rolling models are shown for illustration in Fig. 4.3, however, many other models may be used, such as those shown by Arya et al. [56]. Additionally, future work could apply the principles and methods discussed to predict slip in other rolled patterns created with non-uniform panels. In rolled gossamer patterns, panels are connected continuously along their creases. For the purposes of visualizing and discretizing the slip, the pattern can be imagined as separate strips connected by a discrete number of hinges along the length of the strip, such as the example shown in Fig. 4.1a. This allows the slip at each hinge location to be quantified, although in a continuous

[56] Arya et al., "Crease-free biaxial packaging of thick membranes with slipping folds," 2017.

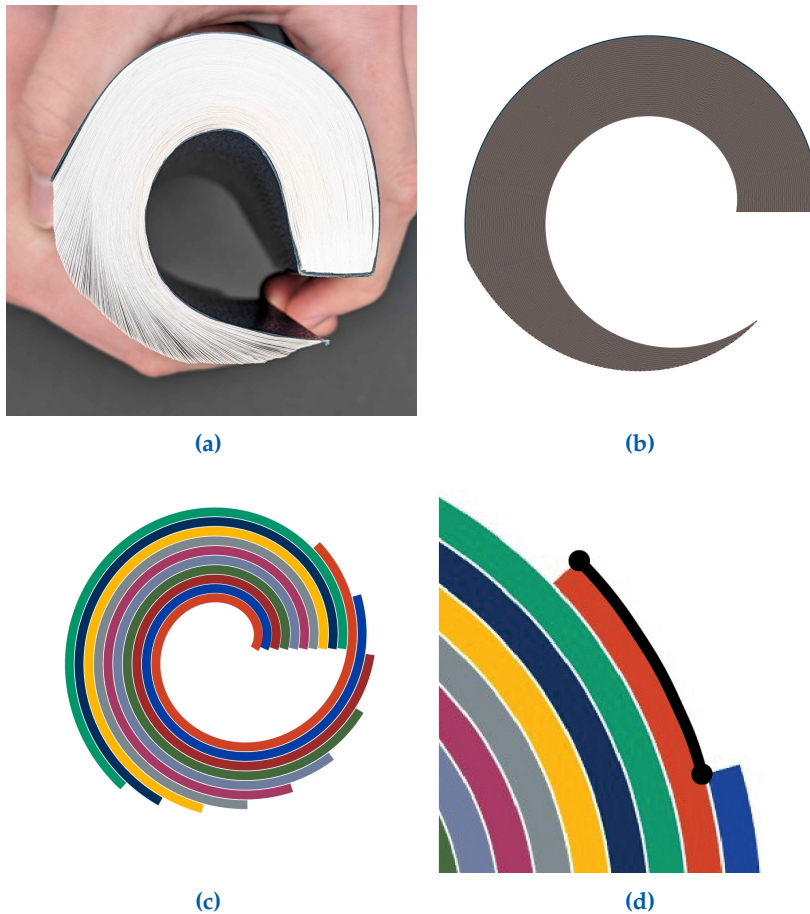


Figure 4.2: Example figure of slipping that occurs during rolling. (a) Rolled book showing slipping between pages. The book shown (The Book of Mormon) has 531 pages. (b) Simulation model of book slippage. Model has 600 panels each with a thickness of 0.02 mm, a total length of 120 mm, and a minimum bend radius of 15 mm, as measured on the book. Because each membrane is so thin, it is difficult to distinguish layers in this example; however the model can be seen to align closely with the physical model, validating the rolling model used. (c) Simple example model to show individual panels. (d) Close-up showing slipping that occurs on the same point between panels in black.

crease joining two strips, this slip could be represented by a continuous curve. In Fig. 4.4a these hinge locations are represented by circles along the length of each strip. It should be noted that this model constrains that each panel is rolled tightly and that gaps are not allowed between panels^a.

The four primary variables used are defined as follows:

- **Number of panels (n):** Any flat array may be divided into n sections. In this work, arrays which are divided into strips are considered, where the width of each strip is defined by the width of the array divided by the number of strips, and the length of each strip is equal to the length of the array, as illustrated in Fig. 4.4a.
- **Thickness of each panel (t):** The thickness of the array. Depending on the purpose of the array, this may be non-uniform, however

^aTo roll a pattern less tightly in this model, the minimum bend radius of the pattern should be increased. This can also be used to simulate the effect of rolling or unrolling the pattern to understand how the slip between panels changes during these events.

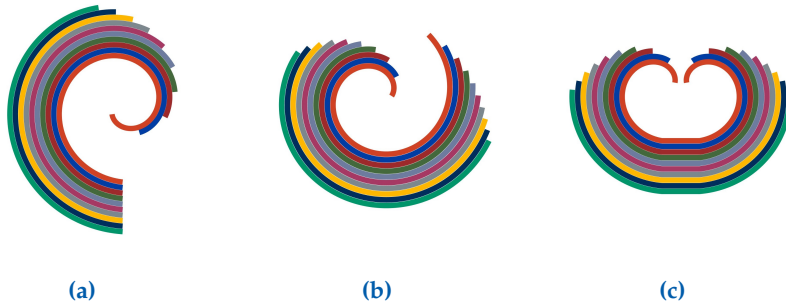


Figure 4.3: Additional rolling models. (a) Exterior aligned, where the outer most edge of each sheet is kept aligned to its adjacent panel. (b) Centered, where the initial angle of each panel in the roll has been adjusted to balance the amount of slipping on each end of a panel, such that the slip on each end is kept equal. This reduces the maximum magnitude of the slippage on any panel. (c) Double roll, where each end is rolled towards the middle.

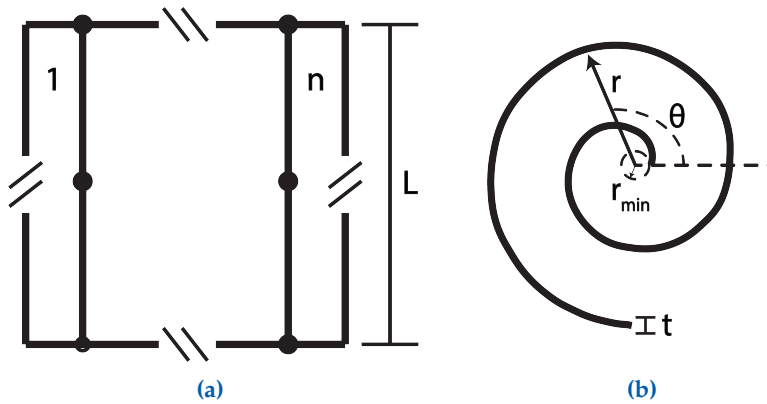


Figure 4.4: General array nomenclature. (a) Number of panels, length, and hinges definition figure. Hinges locations are shown as circles, indicating the point on each panel where slip is being measured. Note that the width of each panel does not affect the slipping between panels, as it is into the plane and does not affect the arc length being measured. (b) Thickness and minimum radius definition.

in this work each panel is considered as having a uniform, equal thickness. Arrays that have an irregular surface may be found to have an effective thickness which can be used in this model; alternatively a more complex implementation could consider each unique thickness separately.

- **Length of each panel (L):** The length of the array. This parameter is the same for each panel.
- **Minimum bend radius (r_{min}):** This is defined by the material properties of the material being rolled, and determines how tightly the array can roll.

In this work, results from the interior aligned model (where the interior edge of each panel is kept aligned), shown in Fig. 4.2c will be shown, because it is the simplest model which illustrates the trends and trade-offs of changing each parameter. Note however, the results shown

apply to each of the alternative models shown in Fig. 4.3. The exterior aligned model (where the exterior edges of each panel are kept aligned), shown in Fig. 4.3a, keeps all of the panel edges on the exterior of the roll aligned and has the edges on the interior of the roll slip relative to each other. The centered roll model, shown in Fig. 4.3b, rolls such that the amount of slipping on each end of a panel is kept equal to reduce the maximum magnitude of the slippage on a panel. Rather than having zero slip on one edge and a maximum slip on the opposite end, each edge experiences half of the maximum slip. There exists a location between each panel where there is no relative slip, however it is more complicated to predict, and so in practice, the double roll is more intuitive and would most likely be a better rolling candidate than the centered roll model. The double roll model, shown in Fig. 4.3c, rolls both outside edges towards the middle, such that the exterior edges slip symmetrically.

4.3.1 Slippage Model

In the following model, polar coordinates were used, where the radius is a function of the input angle. The model is implemented by the following algorithm.

This method verifies that each panel is of the length defined, as shown in Fig. 4.2c. Because the slip between panels is being characterized as points set a prescribed distance away from each edge, the location of each “hinge” in the rolled state may be found using a similar method to

Algorithm 4.1 Rolled Interior Aligned Model Algorithm

```

1: procedure Find positions of panels in roll
2:   Initialize variables  $L, t, n, r_{min}$ 
3:   for  $i \rightarrow 1$  to  $n$  do
4:      $\theta_{final,i} = \theta_{final,i-1} + d\theta$ 
5:      $l = \int_0^{\theta_{final,i}} \sqrt{r^2 + \left(\frac{dr}{d\theta}\right)^2} d\theta$ 
6:     while  $l < L$  do
7:        $\theta_{final,i+} = d\theta$ 
8:        $l = \int_0^{\theta_{final,i+}} \sqrt{r^2 + \left(\frac{dr}{d\theta}\right)^2} d\theta$ 
9:     end while
10:  end for
11:  for  $i \rightarrow 1$  to  $n$  do
12:    Create vector from  $0 \rightarrow \theta_{final,i}$  for panel  $i$ 
13:  end for
14:  for  $i \rightarrow 1$  to  $n$  do
15:    Calculate radii at each point in panel  $i$  using
16:     $r = r_{min} + (i - 1)t + \left(\frac{t}{2}\right)f + \left[\frac{\theta}{2\pi}nt\right]$ 
17:  end for
18:  return  $\theta$  and radii vectors
19: end procedure

```

Algorithm 4.1, however instead of finding a θ_{final} for each panel which resulting in the panel being the correct length, a θ_d which corresponds to each hinge location is found, such that the length is equal to the hinge's distance from the edge of the pattern. This allows the hinge points in the rolled state to be found, and the distance between the same points on adjacent panels to be measured, which is then used to define the slip that occurs at each location. An example of an interior aligned model with hinges is shown in Fig. 4.5. Fig. 4.5b shows the distance between adjacent panels at each hinge location, indicating the amount of slip that is required at each location to enable the gossamer to roll.

The length of a polar curve can be found by

$$l = \int_{\theta_{initial,i}}^{\theta_{final,i}} \sqrt{r^2 + \left(\frac{dr}{d\theta}\right)^2} d\theta \quad (4.1)$$

and the radius of any point is defined by the equation

$$r = r_{min} + (i - 1)t + \left(\frac{t}{2}\right)f + \left[\frac{\theta}{2\pi}nt\right]. \quad (4.2)$$

This equation has several parts. The first three terms consist of determining the initial radius of any sheet, and the fourth term adds the effect of the angle at which the particular coordinate is at. The initial radius of each panel is affected by several factors, such as the minimum bend radius, how many panels are below it in the pattern, as well as the thickness of the material being rolled. The first term (r_{min}) accommodates the minimum bend radius, the second term $((i - 1)t)$ adds the thickness of all of the panels closer to the center than the sheet being found, and the third term $\left(\frac{t}{2}\right)f$ is a factor to find either the top, middle, or bottom surface location of any panel, where $f = 1, 0,$ or -1 for the top, middle, and bottom surfaces, respectively. The fourth term $\left(\frac{\theta}{2\pi}nt\right)$ adds to the radius in proportion to the angle at which any point is at, using the assumption that the radius increases the total thickness of all panels in each full rotation. This is intuitive, as the bottom surface of the innermost panel in a pattern will be in contact with the top surface of the outermost panel when it has made a full rotation. If the radius were smaller after one rotation, the panels would interfere with each other and it would not be able to roll. While some rolled patterns do not make a full rotation, such as that shown in Fig. 4.2b, it is assumed that the radius is continually increasing with this same relationship. Fig. 4.2c shows how, after a rotation of 2π radians, the radius of the innermost panel has been offset from its original value by the sum of the thicknesses of the other panels.

By substituting Equation 4.2 into Equation 4.1, the analytical solution for the length of a sheet of material in a rolled pattern can be found using the following equations:

$$A = n t \quad (4.3)$$

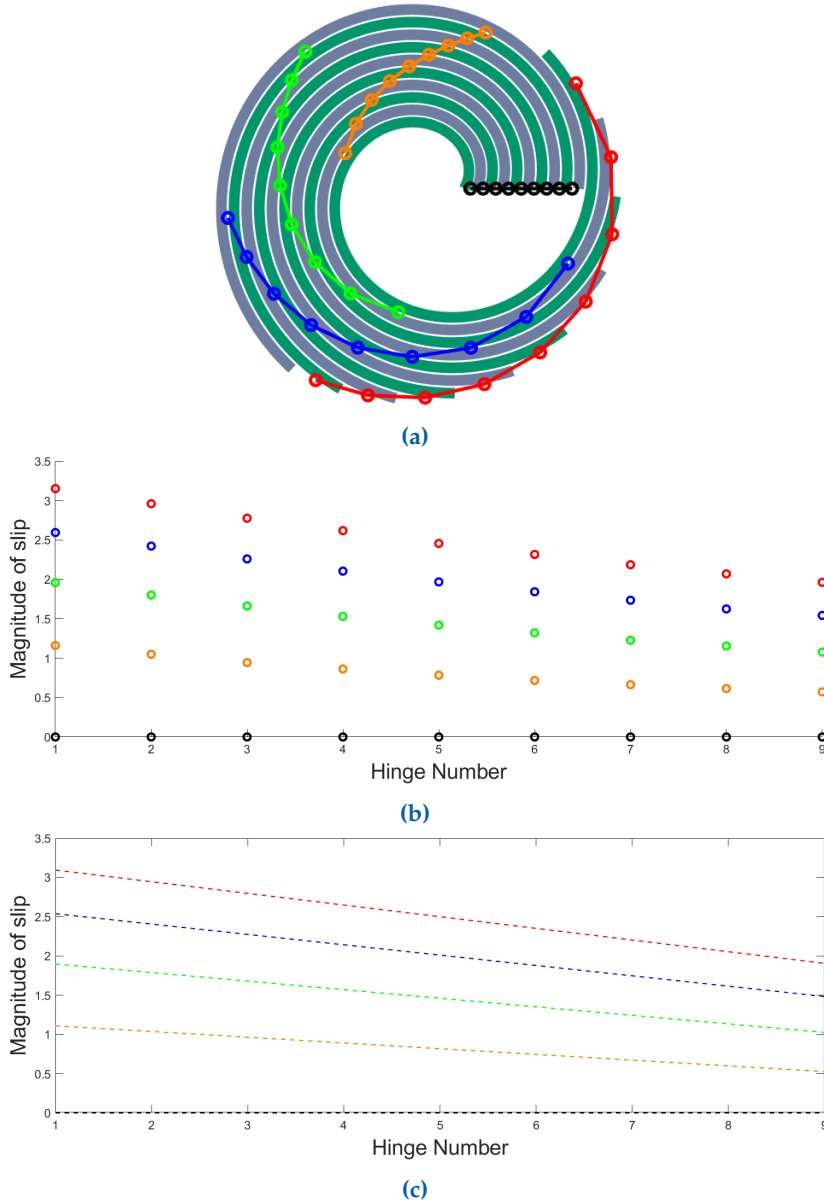


Figure 4.5: Interior aligned model with five hinges. (a) Model with given parameters, with hinge locations shown halfway through the slip measured for adjacent panels. (b) Plot of the magnitude of slip required at each hinge location. (c) Linear fit to the slippage plot.

$$B = r_{min} + t (i - 1) \quad (4.4)$$

$$C = \frac{A^2}{4} + \pi^2 i^2 t^2 - 2 \pi^2 i t^2 + \pi^2 t^2 \quad (4.5)$$

$$D = r_{min}^2 \pi^2 - 2 r_{min} t \pi^2 + 2 r_{min} i t \pi^2 \quad (4.6)$$

$$E = \sqrt{A^2 \theta^2 + A^2 + 4 \pi A B \theta + 4 \pi^2 B^2} \quad (4.7)$$

$$F = E (A \theta + 2 \pi B) \quad (4.8)$$

$$G = \sqrt{A^2 \theta^2 + 4 B \pi A \theta + 4 C + 4 D} \quad (4.9)$$

$$l(\theta) = \left(\frac{1}{4 A \pi} \right) \left[F + A^2 \ln \left(\frac{A^2 \theta + A G + 2 \pi A B}{2 A \pi} \right) \right] \quad (4.10)$$

4.4 Simulation Results

Using this model, the relative displacement between adjacent panels in a rolled pattern can be determined for any point along the panel. This allows for the prediction of the translational motion required when actuating these structures, which is particularly useful when determining appropriate hinges to incorporate into a design.

The four parameters outlined in Section 4.3 determine the final displacement of the rolled model. Using the model, the effect that each of these has on the final design and how to tailor each parameter to modify the overall slippage between panels can be determined.

To visualize the effect of slipping on the model, a number of hinges to be equally spaced along the panel are assigned, and then plot the relative displacement between panels at each hinge location. An example of this is shown in Fig. 4.5. It should be noted that a pattern with n panels will have $n - 1$ hinges. In Fig. 4.5, each hinge location is defined by a distance away from the interior edge, and is represented by a unique color. This facilitates visualization of how the magnitude of the relative displacement between panels increases along each panel as it is further from the aligned edge, as well as how the relative displacement changes along a given hinge location for each panel which is further away from the center of the roll. The two primary parameters that will be used to quantify results are the maximum displacement found within a pattern, as well as the slope of a linear fit to the displacement of each hinge location. The maximum displacement is useful for quantifying how much parasitic motion needs to be incorporated into a design to accommodate slippage between panels. This affects the design of hinges in the pattern and strategies they use. For example, a pattern with a small maximum displacement may incorporate a compliant hinge that achieves precise behavior, while a pattern with more displacement may require a hinge which allows sliding between panels, such as that shown in Section 4.5. More relative displacement required between panels is similar to adding more degrees of freedom to the system, in that more motion and freedom into the system to achieve folding must be introduced. As such, minimizing the magnitude of relative motion between panels is preferred in the scope of this work.

An additional metric for determining the desirability of the configuration is the slope of a linear fit to the displacement along a hinge location. Finding a linear fit to each set of hinges defined by a hinge

location allows the relative range of displacements which are required at each hinge location to be found. The displacement of each hinge location is illustrated in Fig. 4.5c by a line of each color. On this plot, many individual points can be seen, each of which represents an individual hinge in the pattern, and by minimizing the slope of the linear fit shown in Fig. 4.5c, the range of unique displacements required by each hinge in a pattern is reduced. This has the benefit of reducing the number of unique hinges which are required and can significantly simplify the design work required for a pattern.

4.4.1 Maximum Relative Displacement

From this model, it can be seen that the maximum magnitude of displacement is intuitively at the outermost edge of the outermost panel, such as the example shown in Fig. 4.2d.

Color scaled heat maps are used in Fig. 4.6 to visually convey the effect the different parameters have on the maximum displacement of a rolled pattern. Fig. 4.6 shows every combination of the four parameters mentioned in Section 4.3. It should be noted that the units of the input parameters depend on the specific use case; for this reason the values in these charts are unitless. The purpose of these charts is to visually show the relationship between the parameters and maximum slippage rather than quantify specific displacement amounts for future replication. For this reason the actual output values of each configuration are not shown. The heat maps show a positive correlation between increased panel thickness and increased slippage, as well as increased strip length and increased slippage. There is a negative correlation, on the other hand, between both the minimum bend radius and number of panels with the amount of slippage that occurs. Inspection of the heat maps shows that the thickness of each panel has the largest relative effect on the maximum slippage that occurs in the pattern. Designers of rolled gossamer structures can use these heat maps as tools to visualize the relative magnitudes and directions each parameter will have on the slippage of panels when making design decisions.

4.4.2 Linear Fit Relationships

The relationships between each parameter and the slope of the slippage are similar to those of the maximum displacement, in that there is a positive correlation between the thickness and length with increasing slippage, and a negative correlation between the number of panels and the minimum bend radius with increasing slippage. One of the main differences between the effects on the maximum displacement and the slope of the slippage for each hinge location is the rate at which they change with each parameter. For example, it can be seen by comparing Figs. 4.6a and 4.7a, Figs. 4.6d and 4.7d, and Figs. 4.6e and 4.7e, that the number of panels has a greater impact on the slope of the slippage at each hinge location than it does on reducing the maximum slippage in the design.

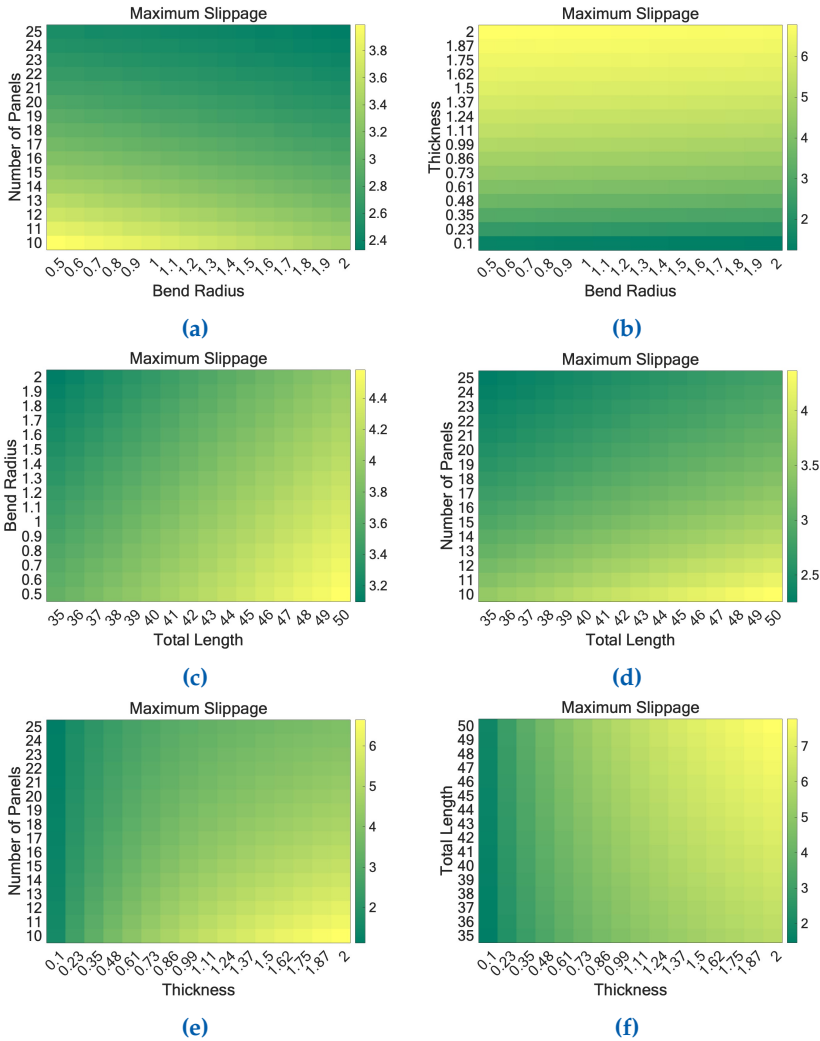


Figure 4.6: Example heat maps showing how the maximum displacement changes for each combination of two parameters. For each combination, there are two parameters that change, and two parameters that are fixed. When fixed parameters are used in this example, there are thickness = 0.5, total length of each panel = 40, minimum bend radius = 1, and number of panels = 10.

4.5 Implementation

To validate the accuracy of the model, an example prototype was made and compared with simulated results, using the double roll model. While the single exterior slip model has been discussed so far, the double roll was chosen for this prototype to demonstrate an example of an additional model. The prototype had the parameters $n = 6$, $r_{min} = 11mm$, $thickness = 0.2mm$, and $L = 600mm$, with 5 hinges along the length. This model is shown in Fig. 4.8a, with the associated magnitude of slip for each hinge shown in Fig. 4.8b. The prototype model was created using hinges which allow for rotation (during folding) and translation (for the slip during rolling), shown in Fig. 4.8d. These hinges were designed specifically to accommodate the slip between panels, because

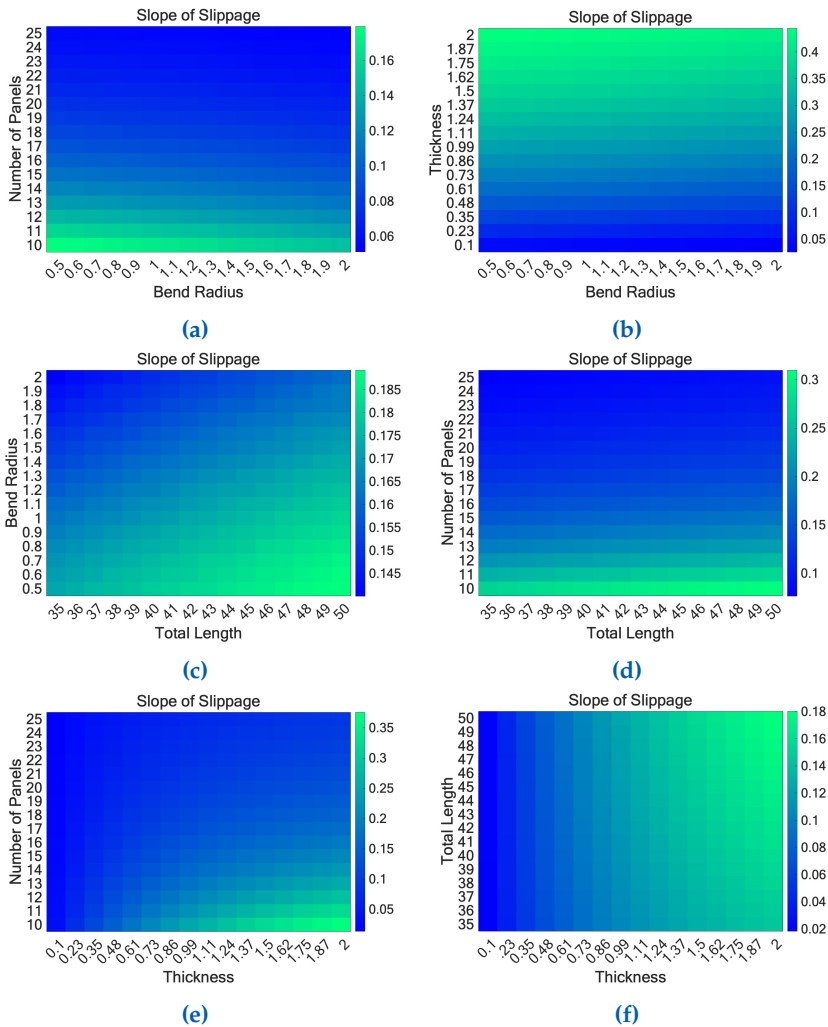


Figure 4.7: Example heat maps showing how the slope of the linear fit changes for each combination of two parameters. For each combination, there are two parameters that change, and two parameters that are fixed. When fixed parameters are used in this example, there are thickness = 0.5, total length of each panel = 40, minimum bend radius = 1, and number of panels = 10.

all other rigid hinges would fail to allow for the sliding required between panels. These hinges are effectively cams which allow motion along the prescribed path. Note that all hinges in the prototype are the same size for simplicity; however, there are adverse effects from introducing a straight hinge into a curved section of material. Being able to accurately predict the maximum displacement at each hinge location allows designers to use the smallest hinges possible at that location, reducing these adverse effects. One method that could be used is to discretize the slip into 3-5 categories, such that each hinge location could use the smallest hinge which would also accommodate the slip required, rather than to create unique hinges for every hinge in the pattern. The prototype double roll is shown in Fig. 4.8c. By measuring the linear displacement at each hinge, the results of the model can be evaluated. For the center hinge,

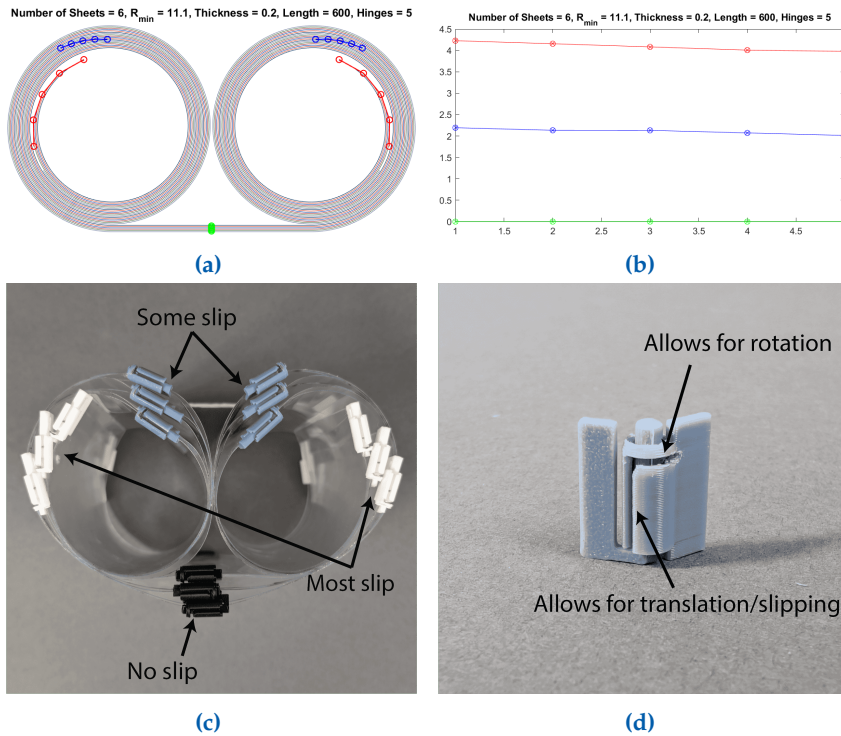


Figure 4.8: Rolling model implementation with example hinges which can be used to accommodate slipping between panels. This model is shown in the open state in Fig. 4.1a. (a) Simulation model with the same parameters. Note that the red hinges in the model correspond to the white hinges in the prototype, the blue hinges in the model correspond to the gray hinges, and the green hinges in the model correspond to the black hinges in the prototype. Hinge colors were changed in the simulation to improve visibility. (b) Slip results for each hinge location in the simulation model. (c) Array in double rolled configuration. Note that the black hinges experience no slip, the gray hinges have some slip, and the white hinges on the outermost edges experience the most slip. (d) Simple hinge used to facilitate rotation and translational motion when stowed.

shown in black, there was no measurable shifting as was expected. For the 3 hinges on each side at an intermediate location, shown in gray, the average shifting was 2.2 mm with a standard deviation of 0.9 mm. This corresponds to the predicted slip of 2.2 mm, with a 2.1% difference between the expected and actual values. The hinges at the outside edge, shown in white, had an average measured slip of 4.3 mm with a standard deviation of 0.7 mm. This corresponds to the predicted slip at the outside edge hinges of 4.3 mm, with a 0.64% difference between the expected and actual values. It should be noted that the friction in the hinges was non-trivial, and that by introducing a stiff linear segment into the rolled model, the results become less accurate. However, it is shown that the model predicted the hinge displacement, and that the methods presented in this paper show promise for use in the design of rolled gossamer structures.

4.6 Conclusion

Gossamer structures are utilized in space applications to minimize stowed volume and maximize deployed surface area. Rolling the membranes that make up gossamer structures reduces wrinkles and creasing but requires relative slipping motion between panels. A numerical model was presented that determines the amount of slipping that occurs between rolled membrane strips, including how it varies across the array in response to changing the variables of thickness, length of the strips, number of panels, and minimum bend radius. This model was verified with a physical prototype, which incorporated hinges that were designed to accommodate for folding and sliding motion. This work is beneficial for future designers of rolled membrane structures, aiding them in the design of appropriate hinges to accommodate relative slipping motion between panels.

The KiHM-9: A Self-deploying PicoSat Antenna Design

5.1 Introduction

High-gain antennas such as parabolic reflectors, phased arrays (PAs), electronically steered arrays (ESAs), reflectarrays (RAs), transmitarrays (TAs), and metasurface antennas (MAs) are commonly used in satellite communication systems and each has its own advantages and disadvantages. For example, PAs can dynamically steer their beams in a desired direction with a high level of beam agility [57]; however, their designs are complex, and they require high-power beam-forming mechanisms that increase both their cost and their profile. TAs and RAs are simple, cost-effective solutions that achieve high gains due to their large apertures, but they have high profile due to the feed source placed several wavelengths away from the reflective surface^a [58]. This chapter is based on work with Mitchel Skinner, Collin Ynchausti, Akash Biswas, Constantinos L. Zekios, Stavros V. Georgakopoulos, Spencer P. Magleby, and Larry L. Howell, which was presented and published with the American Institute of Aeronautics and Astronautics (AIAA) SciTech 2024 Forum session on Small Satellite Deployable Structures [36].

Metasurface antennas, particularly HMAs, have all the advantages of RAs and TAs, while, in addition, they are low-profile structures, making them promising candidates for use in satellite systems. Their performance is achieved using sub-wavelength unit cells (e.g., passive microstrip patch antennas of size $\lambda/5 \times \lambda/5$ as shown in the bottom left inset of Fig. 5.1) properly distributed on their flat apertures, and fed by a single source placed at the center of the HMA's aperture. Despite the attractive electromagnetic properties of all these large aperture high-gain antennas, folding them compactly for transport to space remains challenging. Stowed antennas must be deployed, which often requires peripheral infrastructure, significantly increasing the weight of the system. Due to these factors, reducing the weight of deployable antennas as well as reducing the weight of systems required to deploy the antennas is an important topic of research and focus of design. Current satellites use a variety of methods to deploy and stabilize antennas, including telescoping booms [59, 60], masts [61], exterior frames and trusses [62, 63], stored strain energy in structures and tensioned cables [64], pneumatics [65], and hardstops [66]. These techniques are

[57] Mailloux, *Phased Array Antenna Handbook, Third Edition*, 2017.

^aNotably, state-of-the-art reflectarrays with an aperture surface of $58\lambda^2$, designed to operate at 16 GHz for exhibiting the necessary realized gain of 26.4 dBi, place their feed antennas (e.g. horn antennas) at distance $H_f = 9.4\lambda$ (where, $\lambda = c/f$, f is the frequency of operation of the antenna and c is the speed of light) from the center of their apertures, that corresponds to 17.6cm.

[58] Rubio *et al.*, "A Foldable Reflectarray on a Hexagonal Twist Origami Structure," 2021.

[36] Coleman *et al.*, *The KiHM-9: A Self-Deploying Picosat Holographic Metasurface Antenna (HMA) Design*.

[59] Firth *et al.*, "Advanced Dual-Pull Mechanism for Deployable Spacecraft Booms," 2019.

[60] Block *et al.*, "Ultralight deployable booms for solar sails and other large gossamer structures in space," 2011.

[61] Guoa *et al.*, "Dynamic Characteristic Analysis of Large Space Deployable Articulated Mast," 2011.

[62] Tamura *et al.*, *Deployment Dynamics of Self-deployable Truss Structure Consisting of Bi-convex Booms*.

[63] Webb *et al.*, *Starshade Mechanical Architecture & Technology Effort*, 2016.

[64] Pehrson *et al.*, *Self-Deployable, Self-Stiffening, and Retractable Origami-Based Arrays for Spacecraft*.

[65] Zirbel *et al.*, 2014.

[66] Blandino *et al.*, *Simulating CubeSat Structure Deployment Dynamics*.

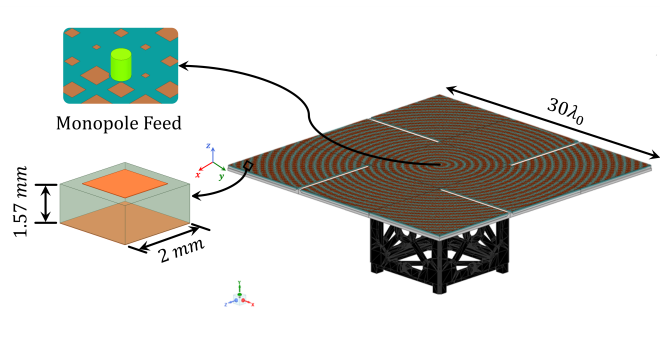


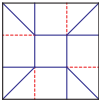
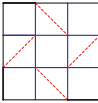
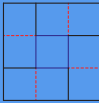
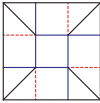
Figure 5.1: Initial deployed holographic metasurface antenna (HMA) concept design with 1U CubeSat structure. In the top left inset, the monopole that feeds the HMA is shown. In the bottom left inset, a 2mm sub-wavelength unit cell is shown consisting of a metallic square patch printed above a grounded substrate with a thickness of 1.57mm.

viable solutions for maintaining the desired performance of antennas; however, some of these techniques require external structures, which occupy payload volume and add mass. These mechanisms are also dependent on hinges and bearings, which can be subject to friction and wear

The objective of this work was to create an HMA that folds around the outside of a CubeSat and incorporates surrogate folds, a stabilization technique, and deployment methods (see Fig. 5.1). The pattern for this antenna was developed with zero-thickness origami models, which were then modified to accommodate the thickness of each panel. The final models considered are shown in Table 5.1, with the model chosen highlighted in blue.

5.2 Design

Table 5.1: Fold pattern candidates based on patterns that can fold around 1U CubeSats. The red dashed lines are valley folds, the blue solid lines are mountain folds, and the interior black solid lines are cuts. The selected pattern is highlighted in blue.

Fold Pattern				
				
Fold Pattern Name	Origami Box with Corner Folds	Four-Sided Flasher	Kirigami 9-Panel	Kirigami 13-Panel
Number of Folds	16	16	8	12
Mountain Folds	12	12	4	8
Valley Folds	4	4	4	4
Number of Cuts	0	0	4	4
Number of Folds and Cuts	16	16	12	16
Rigid-Foldable	Yes	No	Yes	Yes
Special Thickness Accommodation	Yes	Yes	No	No

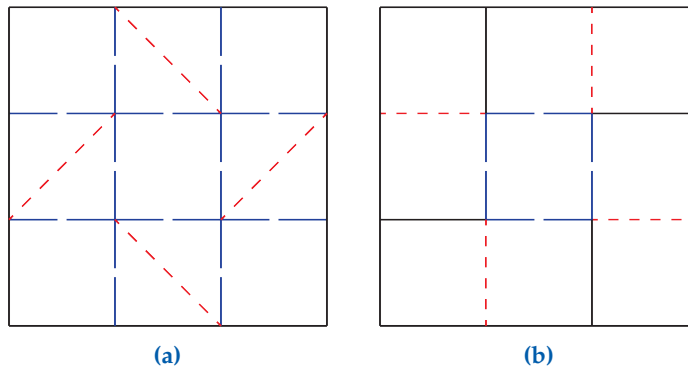


Figure 5.2: (a) Analog flasher pattern with parameters $m=4$, $r=1$, $h=1$, and $dr=0$. Each repeating quadrant is referred to as a “gore”. (b) Associated kirigami flasher pattern. Mountain folds are shown with blue long dashed lines, valley folds are shown with red short dashed lines, and cut lines are shown with black solid lines.

5.2.1 Project Requirements

The aim of this work was to create a foldable metasurface that uses surrogate folds and other components appropriate for the space environment, can function reliably and repeatedly, deploys from a compact stowed area to a large deployed area, and is stable in a deployed configuration.

5.2.2 Pattern Selection

The deployed shape and aspect ratio requirement was for the deployed antenna to fill out a square 9-panel metasurface and to stow compactly on the outer sides of the CubeSat. An example is shown in Fig. 5.1, which shows how the unfolded holographic metasurface antenna would work with a 1U CubeSat structure.

A kirigami flasher pattern was used for its simplicity and variety of folds. This pattern used a flasher pattern with the parameters $m = 4$, $r = 1$, $h = 1$, and $dr = 0$ [22], shown in Fig. 5.2a. The pattern was then modified to reduce the number of total panels and hinges by introducing cuts between gores, as shown in Fig. 5.2b. While modifying the design using kirigami principles introduces more degrees of the freedom to the flasher pattern, it was seen as desirable to reduce the complexity of integrating a pin-less hinge design by reducing the number of folds in the pattern, as well as reducing the number of panels that were manufactured from 13 to 9. Note that each repeating section of a flasher pattern is referred to as a “gore”, and so each of the four repeating sections in this design will also be referred to as such.

[22] Lang *et al.*, “A review of thickness-accommodation techniques in origami-inspired engineering,” 2018.

5.2.3 Embedded Membrane Surrogate Hinges

When origami patterns are thickened to accommodate materials, the paper folds must be replaced with “surrogate folds”. Often, this can be accomplished with a simple pin joint; however, this work sought to incorporate surrogate folds which are appropriate for a space environment and which would not require lubrication. An embedded membrane

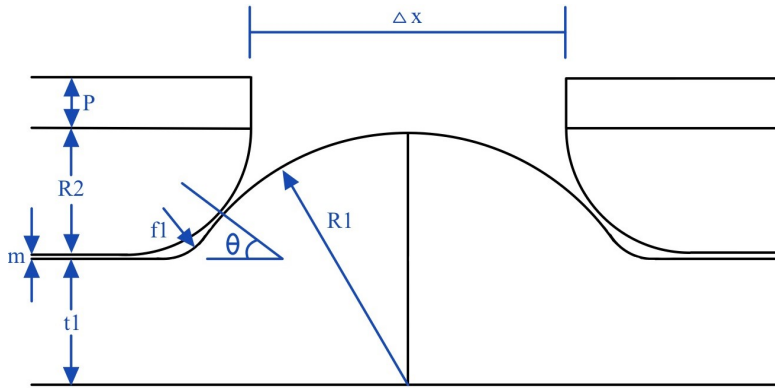


Figure 5.3: Geometry of hinge structure from Ynchausti et al. Note that the thickness of the metasurface antenna panels is given by P , which is added to R_2 to give $R_{2, effective}$.

hinge was chosen for its ability to leave deployed panels on the same plane while maintaining a large usable surface area when deployed.

Embedded Membrane Hinge Geometry

The embedded membrane hinge design chosen was developed by Ynchausti et al. [67] This method uses two contacting circles of different radii to keep the membrane tensioned in both the open and closed positions, building off the Regionally Sandwiching of Compliant Sheets (ReCS) method of sandwiching a membrane between two panels. This modified approach increases control over the stress by varying the radius of the joint, allowing for less stress on the membrane while in a closed state, as shown in Fig. 5.3. When using this design, the larger radius, R_1 , is the limiting factor for the total thickness of the final panels, which in turn determines the weight and volume of the overall antenna. As such, R_1 was designed to be as small as possible, which was determined by the allowable stress in the membrane material. If the radius could be sufficiently thin, the limiting factor on the panel thickness would become the thickness required to achieve sufficient panel stiffness and limit compliance. The stress in the membrane hinge is given by

[67] Ynchausti et al., "Adjustable, Radii-Controlled Embedded Lamina (RadiCEL) Hinges for Folding of Thick Origami-Adapted Systems," 2023.

$$\sigma = \frac{Ec}{R} \quad (5.1)$$

which substituting $\sigma = \frac{Mc}{I}$ into Equation 5.1, when solved for the required radius becomes

$$R \geq \frac{Em}{2S_y} \quad (5.2)$$

where R is the radius of the bend, E is the modulus of elasticity of the membrane material, m is the thickness of the membrane, and S_y is the yield strength of the membrane.

A stainless steel mesh was chosen as the hinge membrane material for its ability to maintain performance in constant exposure to UV radiation. The mesh used is a 306 Stainless Steel 400 mesh which was woven in a non-crimped pattern with a hole diameter of $30 \mu\text{m}$ and a wire diameter

of 0.03 mm. This mesh has a modulus of elasticity of $E = 193$ GPa, a yield strength of $S_y = 290$ MPa, and a thickness of $h = 0.08$ mm. Note that in Fig. 5.3, the thickness of the PCB is added to R_2 to give $R_{2, effective}$. When treating the mesh as a solid membrane and substituting these parameters into Equation 5.2, the radius required to avoid yielding of the material is found to be

$$R \geq 2.66 \text{ cm.} \quad (5.3)$$

This is a relatively large radius considering the scale of the antenna and mesh. However, because of the the nature of the mesh and how it is woven, it differed from a thin solid sheet which is assumed in the stress calculations. Here are a few factors that affect the stress of the stainless steel mesh:

1. The effective modulus of elasticity for a mesh of the same material would likely be different than that of a solid sheet.
2. Each wire in the mesh is not locked in place relative to the other wires around it, allowing it to more equally distribute loads within the mesh.
3. The total thickness of the mesh is greater than the thickness of any single wire being stressed, and so each wire can undergo more deflection before yielding than is predicted if it were the thickness of the mesh.
4. Due to the way the wires are woven over and under each other, the moment and stress applied to each wire are not equal to the moment applied to the mesh, and depend on the position of each wire in the weave. As such, Equation 5.2 is not a constant indicator of the actual maximum radius.
5. When one wire is stressed more than those around it, it can yield until the load is distributed to other wires, dispersing the load and prolonging time to failure due to one weak link.

Because of these considerations, Equation 5.3 can be taken to be an upper limit for R , and to account for these factors, it was estimated that a radius of roughly 25% this size could be used. This resulted in a maximum radius of 0.5 cm, and this choice was verified through fatigue testing, detailed in Section 5.3.1. The geometry of the radius on each panel complicated the manufacturing process and could be optimized in future work for each hinge material chosen. From a maximum radius of 0.5 cm, values are found for each variable, as listed in Table 5.2.

From these design values and using equations presented by Ynchausti et al. [67] for the relationship between radii (R_1, R_2), the angle at which they are placed to each other (θ), and the total thickness (t_1), are calculated as

[67] Ynchausti et al., "Adjustable, Radii-Controlled Embedded Lamina (RadiCEL) Hinges for Folding of Thick Origami-Adapted Systems," 2023.

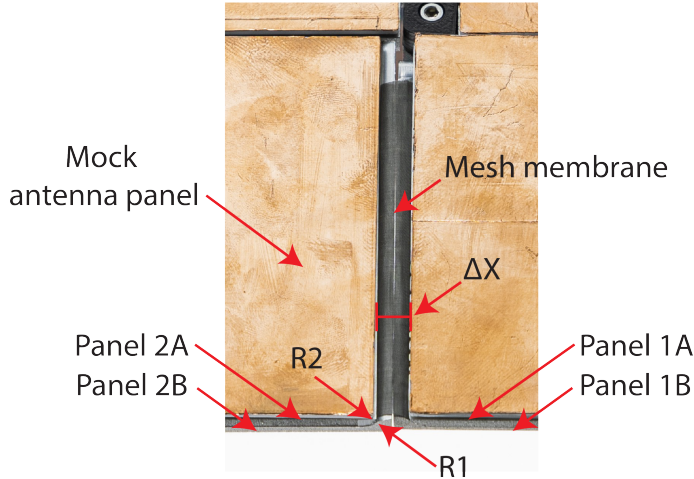


Figure 5.4: Close up of hinge design on final prototype.

$$\theta = \frac{\pi}{2} \left(\frac{R_2}{R_1 + R_2} \right) \quad (5.4)$$

$$t_1 = (R_1 + R_2) \cos(\theta) - R_2 \quad (5.5)$$

Because the PCB panels are relatively thin, and the mesh membrane thickness is negligible, $R_{2, effective}$ becomes $R_2 + P$. This means that for this case θ can be calculated as 40.39° and $t_1 = 0.3995\text{cm}$. With this design, the total surface area was 900cm^2 , with the hinges taking up just 30cm^2 , leaving 870cm^2 or 96.6% of the total area available. Fig. 5.4 shows the hinge design with the calculated geometry from Table 5.2 in the final prototype.

5.2.4 Stability with Magnetic Embedded Hinges

Magnets were selected for use in the stabilization method because of their ability to maintain a constant force over time without being subject to creep or stress relaxation. To keep a low profile, magnets were used

Table 5.2: Geometric variables of designed hinge. Items with an asterisk were given, and not determined through calculation. Note that f_1 is only necessary to facilitate manufacturing of the internal corner at the bottom R_1 .

Variable	Description	Value
R_1	Radius of the bottom panel	0.5 cm
R_2	Radius of the top panel	0.25 cm
f_1^*	Fillet radius	0.2 cm
m^*	Membrane mesh thickness	0.008 cm
P^*	Thickness of reflectarray PCB	0.157 cm
$R_{2, Effective}$	Effective R2	0.407 cm

in a simple bistable configuration with an offset inspired by Pruett et al. [68]. Because there is an offset between magnets, the stability in the stowed state is minimal such that it takes a negligible force to overcome, making the configuration effectively monostable. Integrating this design in the kirigami flasher gains additional stability as the magnets in each gore interlock with the magnets in the two adjacent gores. Although the magnets could be much smaller in practice, as the antenna would not be subject to a constant gravitational force while in orbit, this model sought to demonstrate the effectiveness of a magnetic embedded hinge in achieving stability by supporting the full weight of the panels in the deployed state under Earth's gravity. To verify that the force of the magnets would be sufficient to support the antenna panels, magnets were put into an Instron tensile testing machine. The resulting forces found were then used to calculate that there would be a factor of safety for supporting the panels under earth's gravity of 1.3.

[68] Pruett et al., *Preliminary Concepts for Magnetic Actuation and Stabilization of Origami-Based Arrays*.

5.2.5 Deployment

The flasher pattern, upon which the kirigami pattern is based, has one degree of freedom; however, by adding cuts, seven additional degrees of freedom were introduced.

As the degrees of freedom increase, so does the complexity of incorporating a deployment mechanism. Therefore, to reduce this complexity, an internal deployment system was preferred. Because magnets were already used for stabilization, they appeared to be an ideal method to use for deployment as well; however, the effective range of the magnetic force was insufficient when compared to the travel required by the panels over the course of their deployment. As such, a lenticular fold is integrated in the frame of the CubeSat to act as a spring during deployment.

Lenticular Lock

The lenticular fold is a compliant mechanism that is manufactured in the shape of an Euler spiral, such that when deformed it stores strain energy and can lie flat. A deployable Euler spiral connector which was developed by Yellowhorse et al. [69] was integrated into each side of the CubeSat, as shown in Fig. 5.5. The lenticular fold is placed as far from the hinge as possible, to provide the largest moment arm to deploy the antenna panels. This functions such that the stowed state is an unstable state, and when a burn wire is cut the system will self-deploy. After 90° of motion the inner panels reach their hard stops, and the corner panels continue their motion due to their angular momentum.

[69] Yellowhorse et al., "Deployable lenticular stiffeners for origami-inspired mechanisms," 2018.

5.3 Prototypes and Testing

5.3.1 Fatigue Testing

To validate the hinge membrane selected, the mechanics and fatigue life were first validated using 3D printed panels, after which the final design was created and tested using materials similar to those that would

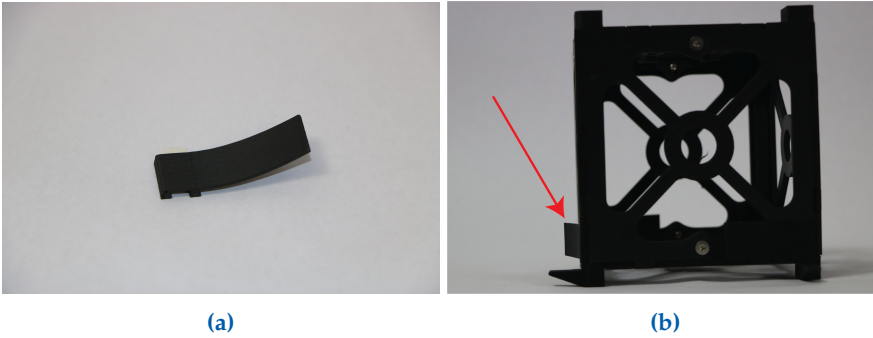


Figure 5.5: (a) Lenticular fold which folds completely flat when stowed and provides an opening force. (b) Side view of the lenticular fold showing its deployed position and displacement relative to a stowed flat position.

be used in space. As shown in Section 5.2.3, there are several unique factors that stem from using a woven mesh as the hinge membrane material as opposed to a uniform sheet material, each of which impact the calculated hinge radius needed to avoid yielding when bending, as given in Equation 5.2. Because of this, the calculated radius (Equation 5.3) is taken to be an upper limit and not a design condition, and a smaller radius was chosen and validated using fatigue testing. Validation was particularly critical for the hinge system before it was integrated into the final design due to the difficulty of precisely predicting mesh performance. A R_1 value of 0.5 cm was chosen and a R_2 value of 0.25 cm was calculated, as shown in Table 5.2.

To test this design, the stainless steel mesh was gripped between two panels and tensioned to 90 N (20 lbf). The joint was then manually cycled 100 times. This testing set-up is shown in Fig. 5.6a. The results of this can be seen in Fig. 5.6b, which shows a 50 times zoom of the mesh at the hinge location. Upon close inspection of the entire joint area, no mesh fibers were found to be broken, and no yielding of local wires could be found. Future work would improve this by testing and creating better models for various membrane hinge materials, so that the radius of the hinge could be more accurately optimized for a given application, resulting in thinner and lighter antennas.

5.3.2 Initial Prototype

A 3D printed model was created to verify design mechanics and behavior, as shown in Fig. 5.7. This model included mock antenna panels with the same thickness as actual panels to validate folding and stowage behaviors. This design also incorporated magnets to verify stabilization behavior.

5.3.3 Manufacturing of Final Prototype

The deployable CubeSat prototype was designed to be as simple as possible, with uniformly shaped panels and common hardware used. The overall process used several manufacturing processes, including waterjet, CNC, and manual milling. Some manufacturing challenges that

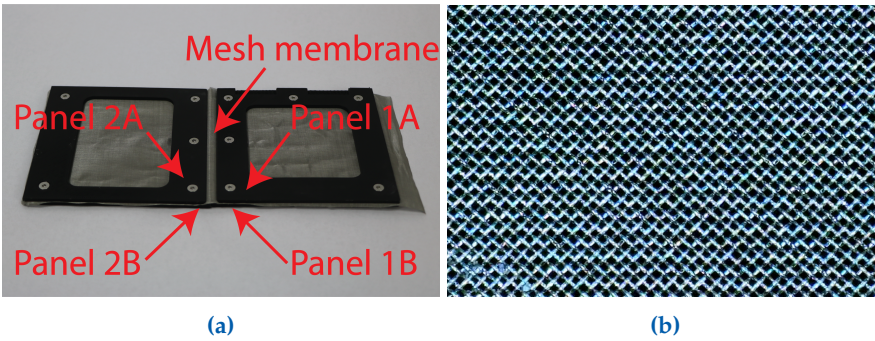


Figure 5.6: (a) Panels used to tension and fatigue test the stainless steel mesh hinge. (b) Close-up photograph from a microscope used to inspect the mesh for material wear and deformation, 50 times zoom, after 100 open-close cycles.

had to be overcome were the thinness of each panel, the varying radii in each panel, and the differing hole placement requirements between different panels. These factors required the use of three separate vacuum table setups, as well as three separate fixture plates. The manufacturing process is described in Appendix B, Table B.1, and each part of the final antenna assembly can be found in the Bill of Materials in Appendix B, Table B.2.

5.4 Results

5.4.1 Final Model

Following assembly, the deployable structure was placed in a micro-gravity simulation, as shown in Fig. 5.8b. The flatness indicates that the magnetic hinges and hard stops were successful in stabilizing the deployable structure in the desired position and that the magnets used to interlock each gore to the next were effective in keeping each gore in the correct position relative to the gore next to it. There are several areas where future work could improve the results of this design. Epoxy was used to keep the magnets in place, and mechanical fasteners are recommended for future models for a more secure connection. Additionally, the mesh hinges, which were held in place by the clamping force of the top and bottom panels, were noted to slip when left for extended periods of time, which would not be an issue in the zero-gravity environment of space, but which is nonetheless an undesired behavior, and could be reduced by using epoxy in addition to the clamping force, to further secure the mesh within the panels. The antenna panels could also be made using forged carbon fiber, which may allow for easier manufacturing of the panel radii and production at scale.

5.4.2 RF Testing

Once the mechanical performance was validated, the mock antenna panels were replaced with the final holographic metasurface antenna (HMA) prototype. In turn, the performance of the HMA was evaluated through design in ANSYS HFSS and prototype measurements in a

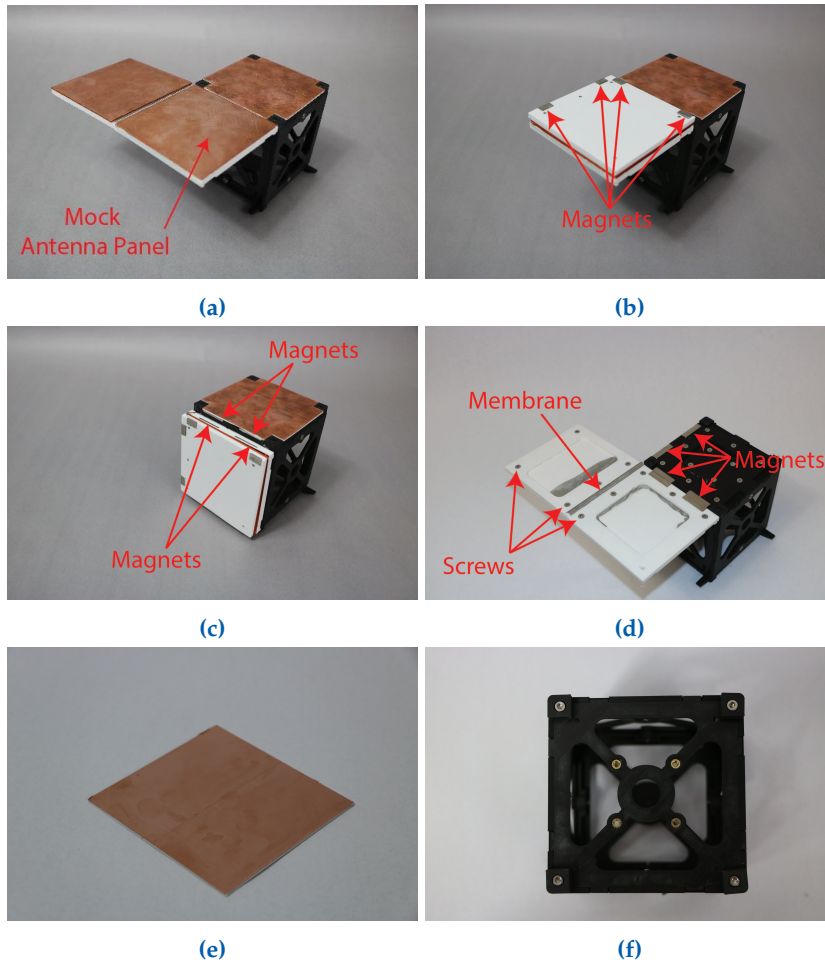


Figure 5.7: The initial CubeSat prototype with deployable antenna structure, shown with one of its four gores attached. (a) Deployed structure with mock antenna panels attached. (b) Mock panels half-closed. The smaller magnets used for stabilization between panels are shown. (c) Mock panels stowed. The larger magnets used for stabilization between each gore to the CubeSat are shown. Note that all panels except for the central top panel are covered and protected during stowage. (d) Deployed structure with mock antenna panels removed to show screw attachment locations. Note the cutout in each of the 1a and 2a panels (defined in Appendix B, Fig. B.1) to reduce the weight of the overall structure as well as to tension the mesh during assembly. (e) Mock antenna panel with the same thickness as the proposed holographic metasurface antenna panels. (f) CubeSat attachment points on the top of the CubeSat. Threads are made with brass inserts in the 3D-printed CubeSat model.

standard anechoic chamber. Notably, two HMA designs of electrical size $30\lambda \times 30\lambda$ were modeled^b, fabricated and measured; (1) an HMA design with no hinges (see Fig. 5.9a) that was used as a reference, and (2) a foldable HMA design comprised of 9 separate panels and 4 rectangular cuts of size $\Delta x = 5.5$ mm properly designed to accommodate the area of the hinges designed in Section 5.2.3 (see Figs. 5.3 and 5.9d). Aiming towards a circularly polarized broadside beam which is essential in satellite communications, a concentric circle-based holographic pattern was properly designed, as depicted in Fig. 5.9a. To feed the HMA,

^bBoth HMA designs were designed to operate at $f = 30$ GHz; $\lambda = c/f$, $c = 3 \times 10^8$ m/s

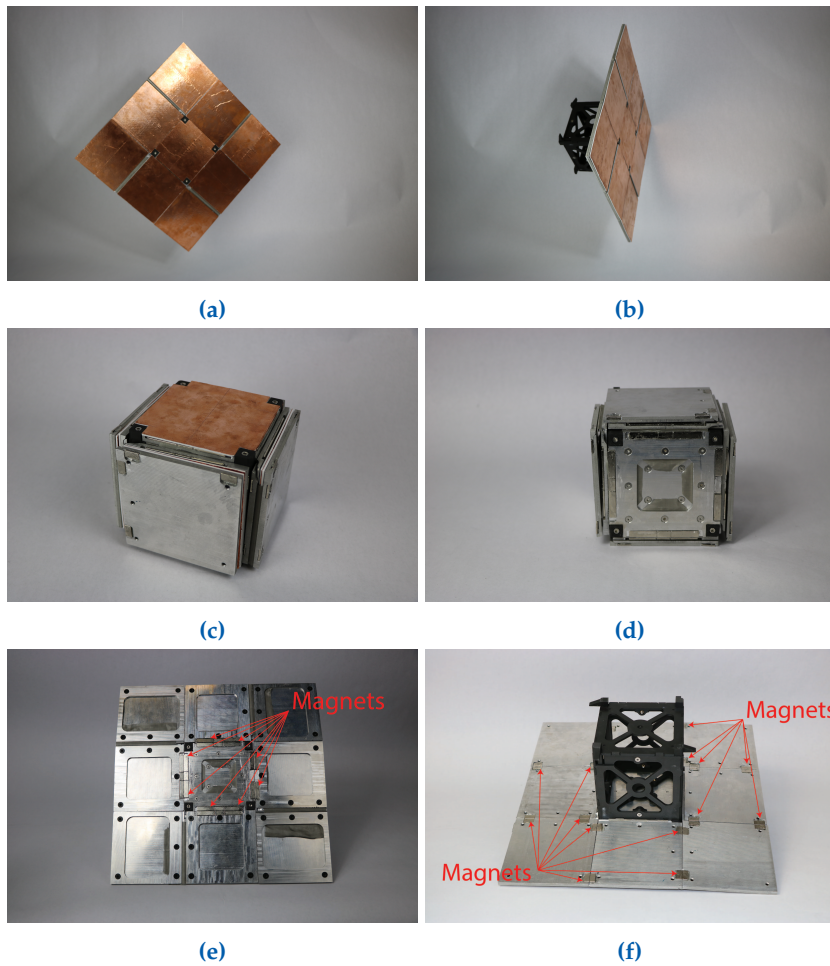


Figure 5.8: The final CubeSat prototype with deployable mock antenna panels shown with all four gores attached. (a) The structure in the deployed configuration, shows a full pattern with 9 mock antenna panels. Note the high area-use efficiency. (b) The structure in deployed configuration, side view. Note that in micro-gravity the mock antenna structure achieves remarkable flatness using the magnets for stabilization and panel thickness as hard stops. (c) Stowed structure. A burn wire would be used to delay deployment until desired, and all panels besides the central panel are covered until deployed. (d) The final structure with mock antenna panels removed, showing the top geometry holding the mesh in place and the magnet placement on the center panel. (e) Final structure with mock antenna panels removed showing the geometry of each panel in the pattern. (f) Bottom view of the final antenna showing magnet placement underneath each panel, which is used to interlock and stabilize each gore.

a monopole antenna was used, placed at the center of the radiating aperture and powered by a coaxial cable connected at the back side of the panel (see inset of Fig. 5.9a. Figs. 5.9b and 5.9e shows two fabricated prototypes placed inside a MVG MicroLab anechoic chamber [70], while Figs. 5.9c and 5.9f show the corresponding measured normalized 2D realized gains. Notably, the HMA without the hinges achieved a total realized gain of 30 dBi, while the deployed HMA achieved 27 dBi. The 3 dB difference between these results is attributed to fabrication errors, and alignment imperfections when the HMA panels were placed on

[70] Group, *Testing Connectivity for a Wireless World*, 2023.

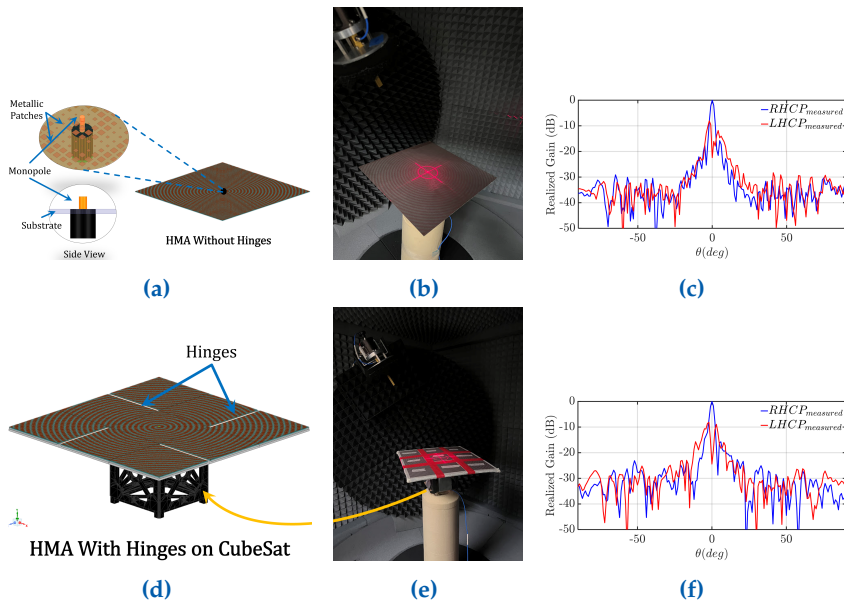


Figure 5.9: (a) A holographic metasurface antenna without hinges; At the inset, the monopole that feeds the HMA is shown in a zoomed view. (b) Measurement setup, and (c) 2D normalized radiation pattern of the HMA prototype without hinges. (d) A fully deployed holographic metasurface antenna mounted on a CubeSat prototype. (e) Measurement setup, and (f) 2D normalized radiation pattern of the fully deployed HMA prototype mounted on a CubeSat prototype.

the deployable structure assembled on the CubeSat. Nevertheless, the gain of 27 dBi fulfills the required nominal gain for establishing reliable communication between a terrestrial base station and a CubeSat.

5.5 Conclusion

The design and manufacture of the KiHM-9 antenna demonstrates the effectiveness and potential of using various technologies, as well as using origami as a starting point for pattern selection. This design validated the performance of magnetic embedded hinges as a method of stabilizing a deployable array without the need for active elements. It also demonstrated the feasibility of embedded membrane hinges as surrogates for zero-thickness models and discusses ways that they might improve in the future. RF testing of the final prototype showed an acceptable level of gain when compared to the simulated results, further validating the capability of the technologies. These technologies combined serve to reduce the peripherals required for deployment and stabilization.

The KiHM-9 shows the potential for future work in this area. Several areas of profitable research for the future stemming from this work are optimizing the hinge radius on the embedded membrane hinge design used by creating better stress and fatigue models for materials used in membrane hinges and exploring different manufacturing methods and materials for the radius hinge design. Additionally, future work could

benefit by experimenting with other methods of securing components, such as adding epoxy to keep the mesh membrane from slipping when stowed and mechanically securing the magnets rather than relying solely on adhesives. Other methods of manufacturing could be explored to facilitate the production of the different radii in the hinge design.

By following the methodology laid out in this work and employing the technologies shown herein, designers can create self-deploying and self-stabilizing space-based holographic metasurface antennas.

Conclusion

In this work, several additions to the body of research on deployable space-based systems were presented. A framework for optimizing rigid-foldable origami patterns was shown, which allows for compliance in the system to mitigate issues during the folding process, such as binding. That work used both a modified model of the origami flasher pattern using frame elements in place of panels, and a surrogate model for a simply supported beam to model the stiffness of each frame element to allow an optimization algorithm to create structures using a variety of frame configurations. That resulted in several unique frame designs, which allow for compliance where required for deployment and folding of the system. Based on this, optimization can be seen to be a valuable tool for the design and improvement of systems based on origami patterns. The resulting designs are unintuitive, and so the use of optimization methods is shown to be beneficial to discover design ideas and concepts which would otherwise remain unknown.

A methodology for designing unique deployable arrays was shown, which uses Hamiltonian circuits and kirigami to create systems which stow with high efficiency and deploy to a predictable shape. The steps for designing these kirigami systems were described, and an example application was given to show how multiple results could be created to fill the project requirements, as well as how those designs can be compared and selected. Based on this, the design space for deployable systems can be seen to have room for more growth, rather than exclusively relying on a subset of commonly used origami patterns. The design space created using this methodology yields exciting results and has immense potential for future applications, based on its simple thickness accommodation, high stowage efficiency, and predictable deployed area efficiency.

A model for the relative motion between adjacent panels in rolled gossamer arrays was shown, with the results being used to examine tradeoffs and considerations between driving parameters. Gossamer structures are used in space applications because they are lightweight and can deploy to large areas from small volumes. Slippage between rolled panels is a characteristic of these arrays which precludes the use of common elements such as rigid hinges, and so the ability to predict this slip allows designers to accommodate it more accurately in their designs. This research showed that the number of panels and thickness of each panel were the most significant parameters to the slip between

panels, while the minimum bend radius of the material and total length of the array were important but less impactful.

Finally, an antenna design was shown which was based on an origami pattern and incorporated frictionless hinges, magnetic stabilization, and deployment from compliant mechanisms. Each incorporated technology was described, and a prototype was created from space-grade materials. The resulting array was then tested in an anechoic chamber, validating the performance of the array for RF applications. This research showed the potential of each of the technologies incorporated, including the origami pattern selected. It also validated the effectiveness of these to create deployable systems which are suitable for the performance requirements in space.

Future work can build on this research in several ways. First, when applying optimization techniques to origami designs, patterns could benefit by allowing for the use any of the three frame designs on a per-panel basis, effectively adding an additional discrete parameter to the optimization. Additionally, it would be beneficial to validate the full pattern optimization results using finite element analysis and prototyping.

Second, future research could explore the possibility of designing kirigami patterns based on uneven stacking of panels, and then thickening certain panels by incorporating additional satellite components into them. This could allow for additional volume efficiency in a design by reducing or eliminating the need for a satellite body, and instead integrate all of the necessary components into the deployable array itself. It may also be useful to consider applications of the Hamiltonian circuit methodology which are designed to tessellate in space. This could facilitate the growth and replacement of components in space.

Third, models for rolled gossamer slip could be expanded by modeling the relative motion between panels in the form of an Archimedean spiral. This would allow the model to take advantage of existing formulas for Archimedean spirals and potentially simplify the computations required. Other work that would facilitate the use of rolled gossamer structures is research into and design of hinges which both allow for the motion required and maintain the benefits of rolled structures.

Fourth, creating better models for the fatigue life of membranes which can be used as hinges would allow for better predictions of their minimum bend radius. Minimizing the radius required during bending would allow designers to make panels using the hinge design demonstrated in the KiHM-9 as small as possible, significantly reducing the mass required in the design.

References

- [1] NASA, *James Webb Space Telescope*, 2024. URL: <https://webb.nasa.gov/content/about/index.html>. cited on p. 1
- [2] ESA, *Euclid*. URL: <https://sci.esa.int/web/euclid>. cited on p. 1
- [3] NASA, *Europa*, June 2014. URL: <https://europa.nasa.gov/>. cited on p. 1
- [4] ESA, *Cheops*. URL: https://www.esa.int/Science_Exploration/Space_Science/Cheops. cited on p. 1
- [5] NASA, *Mars Reconnaissance Orbiter*, 2024. URL: <https://www.nasa.gov/image-article/mars-reconnaissance-orbiter-mro/>. cited on p. 1
- [6] —, *Lunar Reconnaissance Orbiter*, 2024. URL: <https://www.nasa.gov/image-article/lunar-reconnaissance-orbiter-lro/>. cited on p. 1
- [7] Outer Space Affairs, U. N. O. for, *Online Index of Objects Launched into Outer Space*, January 2024. URL: <https://ourworldindata.org/grapher/yearly-number-of-objects-launched-into-outer-space?time=2003..latest>. cited on p. 1
- [8] Salas, E. B., *Number of satellites launched by year 2019*, March 2022. URL: <https://www.statista.com/statistics/896699/number-of-satellites-launched-by-year/>. cited on p. 1
- [9] Rahmat-Samii, Y., Manohar, V., and Kovitz, J. M., “For satellites, think small, dream big: A review of recent antenna developments for cubesats.” *IEEE Antennas and Propagation Magazine*, vol. 59, no. 2, 2017, pp. 22–30. cited on p. 1
- [10] Kaddour, A.-S., Velez, C. A., Hamza, M., Brown, N. C., Ynchausti, C., Magleby, S. P., Howell, L. L., and Georgakopoulos, S. V., “A foldable and reconfigurable monolithic reflectarray for space applications,” *IEEE Access*, vol. 8, 2020, pp. 219 355–219 366. cited on p. 1
- [11] Filipov, E. T., Tachi, T., and Paulino, G. H., “Origami tubes assembled into stiff, yet reconfigurable structures and metamaterials,” *Proceedings of the National Academy of Sciences*, vol. 112, no. 40, 2015, pp. 12 321–12 326. cited on pp. 1, 4
- [12] Kuribayashi, K., Tsuchiya, K., You, Z., Tomus, D., Umemoto, M., Ito, T., and Sasaki, M., “Self-deployable origami stent grafts as a biomedical application of ni-rich tini shape memory alloy foil,” *Materials Science and Engineering: A*, vol. 419, no. 1, 2006, pp. 131–137. cited on pp. 1, 4
- [13] Pehrson, N. A., Ames, D. C., Smith, S. P., Magleby, S. P., and Arya, M., *Self-deployable, self-stiffening, and retractable origami-based arrays for spacecraft*, 2020. cited on pp. 1, 4

- [14] Liu, X., Georgakopoulos, S. V., and Rao, S., "A design of an origami reconfigurable qha with a foldable reflector [antenna applications corner]," *IEEE Antennas and Propagation Magazine*, vol. 59, no. 4, 2017, pp. 78–105. cited on pp. 1, 4
- [15] Kaddour, A.-S., Zekios, C. L., and Georgakopoulos, S. V., "A reconfigurable origami reflectarray," *2020 14th European Conference on Antennas and Propagation (EuCAP)*, IEEE, 2020, pp. 1–4. cited on pp. 1, 4
- [16] Russo, N. E., Zekios, C. L., and Georgakopoulos, S. V., "A capacity reconfigurable multimode origami mimo antenna," *2019 IEEE International Symposium on Antennas and Propagation and USNC-URSI Radio Science Meeting*, IEEE, 2019, pp. 411–412. cited on pp. 1, 4
- [17] Lee, S., Shah, S. I. H., Lee, H. L., and Lim, S., "Frequency-reconfigurable antenna inspired by origami flasher," *IEEE Antennas and Wireless Propagation Letters*, vol. 18, no. 8, 2019, pp. 1691–1695. cited on pp. 1, 4, 7
- [18] Zirbel, S. A., Lang, R. J., Thomson, M. W., Sigel, D. A., Walkemeyer, P. E., Trease, B. P., Magleby, S. P., and Howell, L. L., "Accommodating thickness in origami-based deployable arrays," *Journal of Mechanical Design*, vol. 135, no. 11, 2013. cited on pp. 1, 4–6
- [19] Guang, C. and Yang, Y., "An approach to designing deployable mechanisms based on rigid modified origami flashers," *Journal of Mechanical Design*, vol. 140, no. 8, 2018. cited on pp. 1, 4, 5
- [20] Howell, L. L., *Compliant mechanisms*. John Wiley & Sons, 2001. cited on pp. 1, 4, 7, 9
- [21] *A Framework for Origami Flasher Pattern Optimization to Mitigate Rigid-Foldability Issues*, vol. Volume 8: 47th Mechanisms and Robotics Conference (MR), ser. International Design Engineering Technical Conferences and Computers and Information in Engineering Conference, August 2023, V008T08A050. DOI: 10.1115/detc2023-116542 cited on pp. 2, 4
- [22] Lang, R. J., Tolman, K. A., Crampton, E. B., Magleby, S. P., and Howell, L. L., "A review of thickness-accommodation techniques in origami-inspired engineering," *Applied Mechanics Reviews*, vol. 70, no. 1, 2018. cited on pp. 2, 5, 18, 48
- [23] *A Preliminary Approach to Select an Origami Source Pattern for Deployable Space Arrays*, vol. Volume 7: 46th Mechanisms and Robotics Conference (MR), ser. International Design Engineering Technical Conferences and Computers and Information in Engineering Conference, August 2022, V007T07A070. DOI: 10.1115/detc2022-90033 cited on pp. 2, 18
- [24] *A Methodology for Designing and Improving Novel Kirigami Patterns using the Hamiltonian Circuit Framework (In-Review)*, 2024, pp. 1–10. cited on pp. 2, 18
- [25] Jenkins, C. H., *Gossamer spacecraft: Membrane and inflatable structures technology for space applications*. American Institute of Aeronautics and Astronautics, 2001. cited on p. 2
- [26] Chandra, M., Kumar, S., Chattopadhyaya, S., Chatterjee, S., and Kumar, P., "A review on developments of deployable membrane-based reflector antennas," *Advances in Space Research*, vol. 68, no. 9, 2021, pp. 3749–3764. cited on p. 3
- [27] Arya, M., Lee, N., and Pellegrino, S., "Ultralight structures for space solar power satellites," *3rd AIAA Spacecraft Structures Conference*, 2016, p. 1950. cited on pp. 3, 33

- [28] Fang, H., Lou, M., Huang, J., Hsia, L.-M., Quijano, U., Pelaez, G., and Svolopoulos, V., "Development of a 7-meter inflatable reflectarray antenna," *45th AIAA/ASME/ASCE/AHS/ASC Structures, Structural Dynamics & Materials Conference*, 2004, p. 1502. cited on pp. 3, 33
- [29] Seefeldt, P., Spietz, P., Sproewitz, T., Grundmann, J. T., Hillebrandt, M., Hobbie, C., Ruffer, M., Straubel, M., Tóth, N., and Zander, M., "Gossamer-1: Mission concept and technology for a controlled deployment of gossamer spacecraft," *Advances in Space Research*, vol. 59, no. 1, 2017, pp. 434–456. cited on p. 3
- [30] Ruggiero, E. J. and Inman, D. J., "Gossamer spacecraft: Recent trends in design, analysis, experimentation, and control," *Journal of Spacecraft and Rockets*, vol. 43, no. 1, 2006, pp. 10–24. cited on p. 3
- [31] Furuya, H., Mori, O., Sawada, H., Okuizum, N., Shirasawa, Y., Natori, M., Miyazaki, Y., and Matunaga, S., "Manufacturing and folding of solar sail 'ikaros'," *52nd AIAA/ASME/ASCE/AHS/ASC Structures, Structural Dynamics and Materials Conference 19th AIAA/ASME/AHS Adaptive Structures Conference 13t*, 2011, p. 1967. cited on p. 3
- [32] *Modeling and Analysis of Inter-Panel Slipping for the Design of Rolled Gossamer Arrays (In-Review)*, vol. 48th Mechanisms and Robotics Conference (MR), ser. International Design Engineering Technical Conferences and Computers and Information in Engineering Conference, August 2024. cited on pp. 3, 33
- [33] Toorian, A., Diaz, K., and Lee, S., "The cubesat approach to space access," 2008, pp. 1–14. DOI: 10.1109/aero.2008.4526293 cited on p. 3
- [34] Lokman, A. H., Soh, P. J., Azemi, S. N., Lago, H., Podilchak, S. K., Chalermwisutkul, S., Jamlos, M. F., Al-Hadi, A. A., Akkaraekthalin, P., and Gao, S., "A review of antennas for picosatellite applications," *International Journal of Antennas and Propagation*, vol. 2017, 2017. cited on p. 3
- [35] Liu, Z.-Q., Qiu, H., Li, X., and Yang, S.-L., "Review of large spacecraft deployable membrane antenna structures," *Chinese Journal of Mechanical Engineering*, vol. 30, no. 6, 2017, pp. 1447–1459. cited on p. 3
- [36] *The KIHM-9: A Self-Deploying Picosat Holographic Metasurface Antenna (HMA) Design*. DOI: 10.2514/6.2024-1429 cited on pp. 3, 46
- [37] Srinivas, V. and Harne, R. L., "Directing acoustic energy by flasher-based origami inspired arrays," *The Journal of the Acoustical Society of America*, vol. 148, no. 5, 2020, pp. 2935–2944. cited on p. 5
- [38] Lang, R. J., Magleby, S., and Howell, L., "Single degree-of-freedom rigidly foldable cut origami flashers," *Journal of Mechanisms and Robotics*, vol. 8, no. 3, 2016, p. 031 005. cited on p. 5
- [39] Zirbel, S. A., "Compliant Mechanisms for Deployable Space Systems," English, Ph.D. Dissertation, Brigham Young University, 2014, p. 107. cited on p. 5
- [40] Tachi, T. *et al.*, "Rigid-foldable thick origami," *Origami*, vol. 5, no. 5, 2011, pp. 253–264. cited on p. 5
- [41] Watanabe, N. and Kawaguchi, K.-i., "The method for judging rigid foldability," *Origami*, vol. 4, 2009, pp. 165–174. cited on p. 5

- [42] Akitaya, H., Demaine, E. D., Horiyama, T., Hull, T. C., Ku, J. S., and Tachi, T., "Rigid foldability is np-hard," *ArXiv preprint arXiv:1812.01160*, 2018. cited on p. 5
- [43] Bolanos, D., Varela, K., Sargent, B., Stephen, M. A., Howell, L. L., and Magleby, S. P., "Selecting and optimizing origami flasher pattern configurations for finite-thickness deployable space arrays," *Journal of Mechanical Design*, vol. 145, no. 2, November 2022. DOI: 10.1115/1.4055900 cited on p. 5
- [44] Varela, K., Oliveira, L., Sargent, B., Howell, L. L., and Magleby, S. P., "Thickness accommodation for the flasher origami deployable array," *AIAA SCITECH 2023 Forum*, 2023, p. 0944. cited on pp. 5, 7
- [45] Lang, R., *Tessellatica*, 2021. cited on p. 7
- [46] Lang, R. J., Tolman, K. A., Crampton, E. B., Magleby, S. P., and Howell, L. L., "A review of thickness-accommodation techniques in origami-inspired engineering," *Applied Mechanics Reviews*, vol. 70, no. 1, February 2018, p. 010 805. DOI: 10.1115/1.4039314 cited on p. 18
- [47] Yang, J., Zhang, Y., Chatzis, M. N., and You, Z., "Folding and deploying identical thick panels with spring-loaded hinges," *Extreme Mechanics Letters*, vol. 52, 2022, p. 101 637. DOI: <https://doi.org/10.1016/j.eml.2022.101637> cited on pp. 18, 25
- [48] —, "Data for "folding and deploying identical thick panels with spring-loaded hinges"," *Data in Brief*, vol. 43, 2022, p. 108 388. DOI: <https://doi.org/10.1016/j.dib.2022.108388> cited on p. 18
- [49] *Compactly Folding Rigid Panels With Uniform Thickness Through Origami and Kirigami*, vol. Volume 5B: 43rd Mechanisms and Robotics Conference, ser. International Design Engineering Technical Conferences and Computers and Information in Engineering Conference, August 2019, V05BT07A042. DOI: 10.1115/detc2019-97946 cited on pp. 18, 20
- [50] Yang, F., Zhang, M., Ma, J., You, Z., Yu, Y., Chen, Y., and Paulino, G. H., "Design of single degree-of-freedom triangular resch patterns with thick-panel origami," *Mechanism and Machine Theory*, vol. 169, 2022, p. 104 650. DOI: <https://doi.org/10.1016/j.mechmachtheory.2021.104650> cited on p. 18
- [51] Yang, J., Zhang, X., Chen, Y., and You, Z., "Folding arrays of uniform-thickness panels to compact bundles with a single degree of freedom," *Proceedings of the Royal Society A: Mathematical, Physical and Engineering Sciences*, vol. 478, no. 2261, 2022, p. 20 220 043. DOI: 10.1098/rspa.2022.0043 cited on p. 18
- [52] Hamilton, W., *The Mathematical Papers of Sir William Rowan Hamilton*. The University Press, 2006. cited on p. 19
- [53] Institute, C. M., "P vs np," 2023. cited on p. 20
- [54] Tang, Y., Guo, H., Liu, R., and Deng, Z., "Space membrane wrinkle analytical model based on piecewise stress field," *Thin-Walled Structures*, vol. 189, 2023, p. 110 869. cited on p. 33
- [55] Arya, M., Lee, N., and Pellegrino, S., "Wrapping thick membranes with slipping folds," *2nd AIAA Spacecraft Structures Conference*, 2015, p. 0682. cited on p. 33

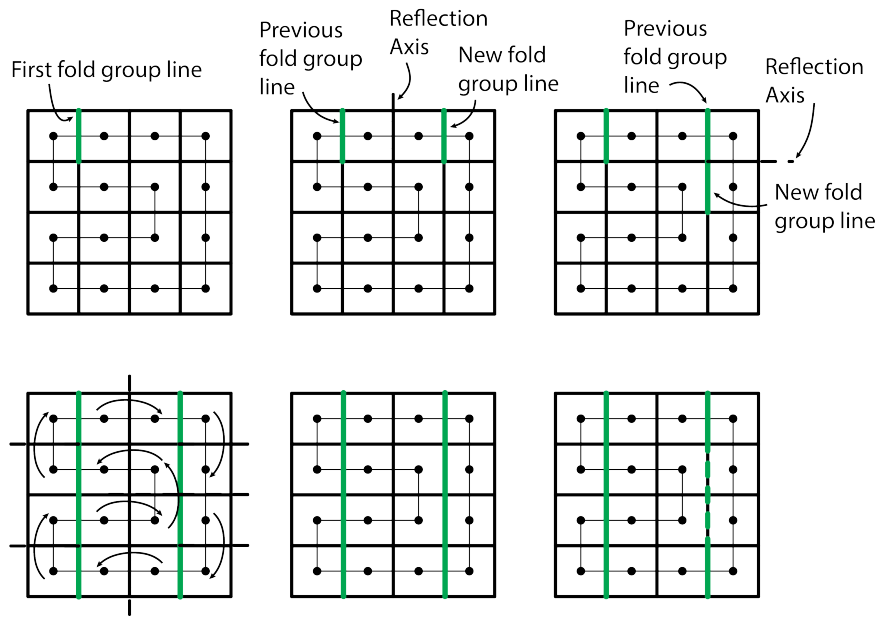
- [56] ———, “Crease-free biaxial packaging of thick membranes with slipping folds,” *International Journal of Solids and Structures*, vol. 108, 2017, pp. 24–39. DOI: <https://doi.org/10.1016/j.ijsolstr.2016.08.013> cited on p. 34
- [57] Mailloux, R. J., *Phased Array Antenna Handbook, Third Edition*, Artech House, 2017. cited on p. 46
- [58] Rubio, A. J., Kaddour, A.-S., Ynchausti, C., Magleby, S., Howell, L. L., and Georgakopoulos, S. V., “A foldable reflectarray on a hexagonal twist origami structure,” *IEEE Open Journal of Antennas and Propagation*, vol. 2, 2021, pp. 1108–1119. DOI: 10.1109/ojap.2021.3127312 cited on p. 46
- [59] Firth, J. A. and Pankow, M. R., “Advanced dual-pull mechanism for deployable spacecraft booms,” *Journal of Spacecraft and Rockets*, vol. 56, no. 2, 2019, pp. 569–576. DOI: 10.2514/1.a34243 cited on p. 46
- [60] Block, J., Straubel, M., and Wiedemann, M., “Ultralight deployable booms for solar sails and other large gossamer structures in space,” *Acta Astronautica*, vol. 68, no. 7, 2011, pp. 984–992. DOI: <https://doi.org/10.1016/j.actaastro.2010.09.005> cited on p. 46
- [61] Guoa, H., Liu, R., Deng, Z., and Zhang, J., “Dynamic characteristic analysis of large space deployable articulated mast,” *Procedia Engineering*, vol. 16, 2011, pp. 716–722. DOI: <https://doi.org/10.1016/j.proeng.2011.08.1146> cited on p. 46
- [62] Tamura, A., Inoue, S., Kawarabayashi, D., Yamazaki, M., and Miyazaki, Y., *Deployment Dynamics of Self-deployable Truss Structure Consisting of Bi-convex Booms* URL: <https://arc.aiaa.org/doi/abs/10.2514/6.2017-0175> cited on p. 46
- [63] Webb, D., Hirsch, B., Bach, V., Sauder, J., Bradford, S., and Thomson, M., *Starshade Mechanical Architecture & Technology Effort*, January 2016 cited on p. 46
- [64] Pehrson, N. A., Smith, S. P., Ames, D. C., Magleby, S. P., and Arya, M., *Self-Deployable, Self-Stiffening, and Retractable Origami-Based Arrays for Spacecraft* URL: <https://arc.aiaa.org/doi/abs/10.2514/6.2019-0484> cited on p. 46
- [65] Zirbel, S., Magleby, S., Trease, B., and Howell, L., *The 42nd Aerospace Mechanism Symposium*. NASA, May 2014. cited on p. 46
- [66] Blandino, J. R., Ross, B., Woo, N., Smith, Z., and McNaul, E., *Simulating CubeSat Structure Deployment Dynamics* URL: <https://arc.aiaa.org/doi/abs/10.2514/6.2018-1677> cited on p. 46
- [67] Ynchausti, C., Shirley, S., Magleby, S. P., and Howell, L. L., “Adjustable, radii-controlled embedded lamina (RadiCEL) hinges for folding of thick origami-adapted systems,” *Mechanism and Machine Theory*, 2023. cited on pp. 49, 50
- [68] Pruet, H., Coleman, N., and Magleby, S. P., *Preliminary Concepts for Magnetic Actuation and Stabilization of Origami-Based Arrays*, American Society of Mechanical Engineers (in review). cited on p. 52
- [69] Yellowhorse, A. and Howell, L. L., “Deployable lenticular stiffeners for origami-inspired mechanisms,” *Mechanics Based Design of Structures and Machines*, vol. 46, no. 5, 2018, pp. 634–649. cited on p. 52
- [70] Group, M. V., *Testing Connectivity for a Wireless World*, accessed: May 2023, 2023. URL: <https://www.mvg-world.com>. cited on p. 56

Appendices

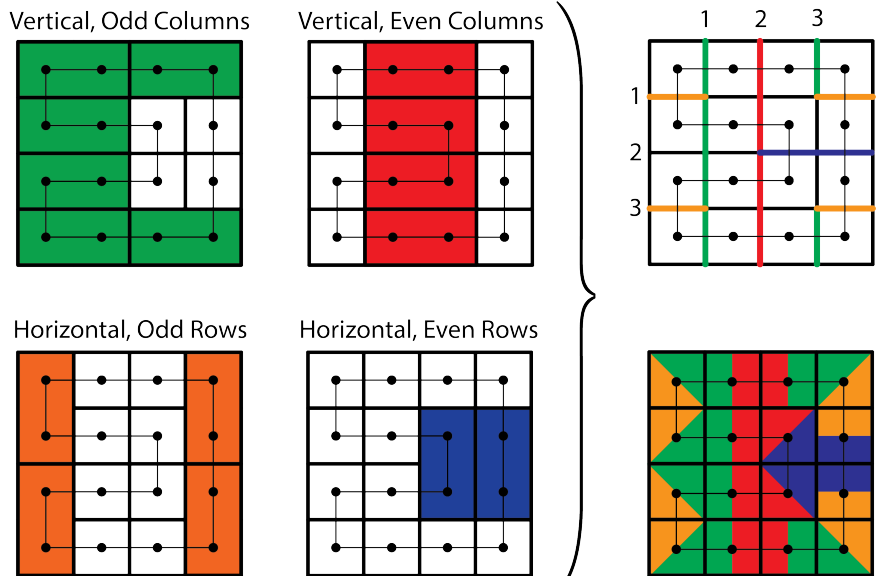
A

Simplified Folding Model for Square-Based Patterns

For patterns based on a grid of square panels, the method for finding the folding groups can be simplified. This is due to the fact that each panel interfaces at exactly 90 degrees to the panels adjacent to it, meaning that reflection sequence follows a predictable pattern. An example of these fold groups is shown in Fig. A.1a. As explained in Chapter 3, there will be four unique folding groups associated with patterns based on squares. These four groups can be seen to fall into four predictable locations; a vertical group which falls on odd numbered rows, a vertical groups which falls on even numbered rows, a horizontal group which falls on odd numbered columns, and a horizontal group which falls on even numbered columns. Thus, when a pattern and corresponding Hamiltonian circuit are chosen, the fold groups can be found by simply sorting the locations where the circuit crosses the pattern into one of the four groups. This is illustrated in Fig. A.1b.



(a)



(b)

Figure A.1: (a) Reflection sequence used to find valid fold groups in square patterns. Fold group lines that do not cross the Hamiltonian circuit and will therefore not be used for folding are shown as dashed. (b) Simplified method shown in squares.

KiHM-9 Manufacturing Details

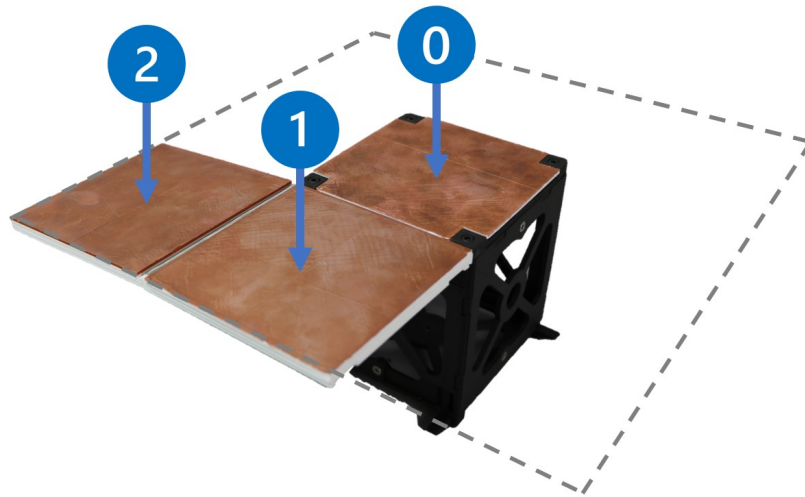


Figure B.1: Numbering nomenclature of the panels during manufacturing. Note that “a” refers the top half of the panel (associated with R_2 on panels 1 and 2) and “b” refers to the bottom half of the panel (associated with R_1 on panels 1 and 2).

Table B.1: KiHM-9 Manufacturing Steps.

Step	Part	Operation	Manufacturing Method
1	All panels	Cut out profile	Waterjet
2	Vacuum plate	Mill	CNC
3	All fixture plates	Mill	CNC
4	All panels, top side	Mill	CNC with vacuum plate
5	All panels, bottom side	Mill	CNC with fixture plate
6	Stainless steel mesh	Cut	Scissors
7	Magnet	Attach	Epoxy
8	All gores	Connect panels	Screw together
9	All gores	Connect to central panel	Screw together
10	Antenna	Connect to CubeSat	Screw together

Table B.2: KiHM-9 Bill of Materials. See Appendix I, Fig. B.1 for nomenclature on panel numbering.

Part	Quantity	Attachment Method
Panel 0A	1	Screws
Panel 0B	1	Screws
Panel 1A	4	Screws
Panel 1B	4	Screws
Panel 2A	4	Screws
Panel 2B	4	Screws
1" by 1/4" by 1/16" Neodymium Magnet	8	Epoxy
1/2" by 1/4" by 1/16" Neodymium Magnet	32	Epoxy
M3x5mm Flat Head Machine Screws	4	N/A
M4x5mm Flat Head Machine Screws	52	N/A
316 Stainless Steel 400 Mesh	1	Friction